iScience

CellPress
OPEN ACCESS

Article

Pandemic-associated pernio harbors footprints of an abortive SARS-CoV-2 infection

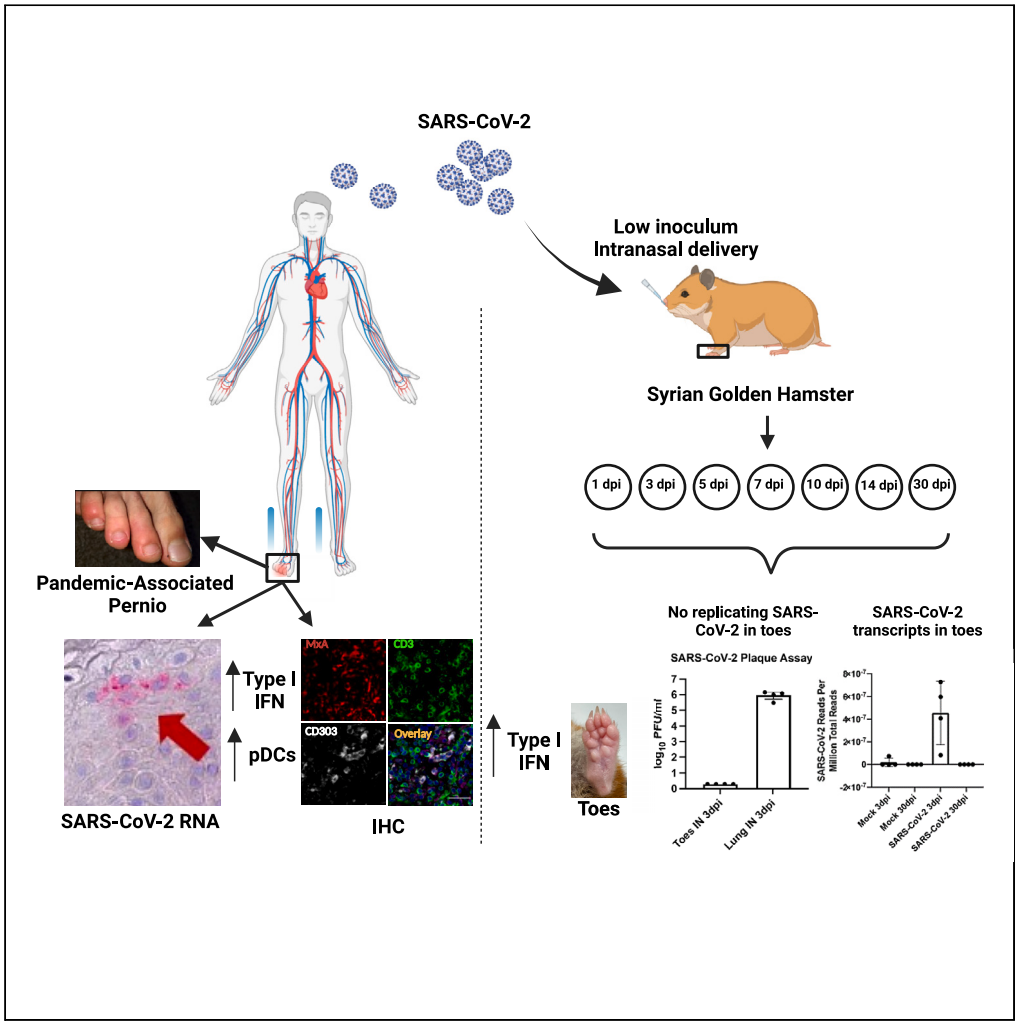

Lisa M. Arkin, Ana C. Costa-da-Silva, Justin Frere, ..., Anne Marie Singh, Benjamin tenOever, Jacqueline W. Mays

jacqueline.mays@nih.gov

Highlights

Pernio skin may contain SARS-CoV-2 viral material, even without seroconversion

Across two pernio cohorts, sparse SARS-CoV-2 RNA was detected in ~25% of biopsies

The local immune profile had plasmacytoid dendritic cells and interferon activity

A golden hamster model replicated disseminated viral RNA without replicating virus

Arkin et al., iScience *27*, 110525
August 16, 2024 Published by Elsevier Inc.
https://doi.org/10.1016/j.isci.2024.110525

iScience

CellPress
OPEN ACCESS

Article

Pandemic-associated pernio harbors footprints of an abortive SARS-CoV-2 infection

Lisa M. Arkin,[1,13] Ana C. Costa-da-Silva,[2,13] Justin Frere,[3,13] Ashley Ng,[1] Rubina Sharma,[2] John J. Moon,[1] Hailey E. Bussan,[4] Clara H. Kim,[2] Ayesha Javaid,[2] Olivia R. Steidl,[5] Ahmad Yatim,[6,7] Fanny Saidoune,[7] Michel Gilliet,[7] Joe T. Nguyen,[2] Aman Nihal,[1] George Luong,[1] Meaghan Kenfield,[1] Lucia Carrau,[3] Jennifer M. Tran,[1] Molly A. Hinshaw,[1] Erin G. Brooks,[4] Jose M. Ayuso,[1] David H. O'Connor,[4] Jean-Laurent Casanova,[6,8,9,10,11] Edward W. Cowen,[12] Beth A. Drolet,[1] Anne Marie Singh,[5] Benjamin tenOever,[3] and Jacqueline W. Mays[2,14,*]

SUMMARY

Elevated pernio incidence was observed during the COVID-19 pandemic. This prospective study enrolled subjects with pandemic-associated pernio in Wisconsin and Switzerland. Because pernio is a cutaneous manifestation of the interferonopathies, and type I interferon (IFN-I) immunity is critical to COVID-19 recovery, we tested the hypothesis that severe acute respiratory syndrome coronavirus 2 (SARS-CoV-2)-mediated IFN-I signaling might underlie some pernio cases. Tissue-level IFN-I activity and plasmacytoid dendritic cell infiltrates were demonstrated in 100% of the Wisconsin cases. Across both cohorts, sparse SARS-CoV-2 RNA was captured in 25% (6/22) of biopsies, all with high inflammation. Affected patients lacked adaptive immunity to SARS-CoV-2. A hamster model of intranasal SARS-CoV-2 infection was used as a proof-of-principle experiment: RNA was detected in lungs and toes with IFN-I activity at both the sites, while replicating virus was found only in the lung. These data support a viral trigger for some pernio cases, where sustained local IFN-I activity can be triggered in the absence of seroconversion.

INTRODUCTION

The host type I interferon (IFN-I) response has proven critical in determining the trajectory of COVID-19 infection.[1–6] Life-threatening COVID-19 can be caused by rare variants of deficient Toll-like receptor (TLR) 3- and TLR-7-dependent IFN-I immunity.[5] Neutralizing autoantibodies against IFN-I increase with age and are a predictor of COVID-19 deaths.[7] Conversely, the milder disease observed in children with COVID-19 may be explained, at least in part, by an elevated IFN-I response.[8–10] These latter data are supported by the finding that a single subcutaneous administration of pegylated IFN-lambda significantly reduces severe acute respiratory syndrome coronavirus 2 (SARS-CoV-2) disease severity.[11,12]

Pernio, also known as chilblains, is a rare cutaneous manifestation of the type I interferonopathies, a group of monogenic disorders characterized by constitutively upregulated IFN-I that results in autoinflammation.[13–16] Following the first reports in March 2020 of otherwise healthy individuals, many of them children, with pernio and few extracutaneous symptoms or signs of COVID-19, pandemic-associated pernio (herein referred to as PAP) was widely reported across Europe and the United States,[17–21] where it was quickly termed by the lay press as "COVID toes." Epidemiological studies suggest temporospatial clustering of pernio with confirmed COVID-19 cases[22–24]; however, direct evidence of this relationship is limited, as most pernio patients test negative for SARS-CoV-2 and lack extracutaneous symptoms of infection.[17,25–27] Although several publications have demonstrated a transient, inducible IFN-I response in blood and endothelial alteration with IFN-I polarization in affected tissue,[28–30] multiple studies have demonstrated a limited adaptive immune response to SARS-CoV-2,

[1]School of Medicine and Public Health, University of Wisconsin-Madison, Department of Dermatology, Madison, WI 53726, USA
[2]Oral Immunobiology Unit, National Institute of Dental and Craniofacial Research, National Institutes of Health, Bethesda, MD 20892, USA
[3]Department of Microbiology, New York University, Grossman School of Medicine, New York, NY 10016, USA
[4]School of Medicine and Public Health, University of Wisconsin-Madison, Department of Pathology and Laboratory Medicine, Madison, WI 53726, USA
[5]School of Medicine and Public Health, University of Wisconsin-Madison, Department of Pediatrics, Madison, WI 53726, USA
[6]St. Giles Laboratory of Human Genetics of Infectious Diseases, Rockefeller Branch, The Rockefeller University, New York, NY 10065, USA
[7]Department of Dermatology at the University Hospital CHUV, 1011 Lausanne, Switzerland
[8]University of Paris Cité, Imagine Institute, 75013 Paris, France
[9]Howard Hughes Medical Institute, New York, NY 10065, USA
[10]Lab of Human Genetics of Infectious Diseases, INSERM, Necker Hospital for Sick Children, Paris, France
[11]Department of Pediatrics, Necker Hospital for Sick Children, 75015 Paris, France
[12]Dermatology Branch, National Institute of Arthritis and Musculoskeletal and Skin Diseases, National Institutes of Health, Bethesda, MD 20892, USA
[13]These authors contributed equally
[14]Lead contact
*Correspondence: jacqueline.mays@nih.gov
https://doi.org/10.1016/j.isci.2024.110525

including seroconversion and SARS-CoV-2-specific T cell responses.[22,25–27] This has yielded a dominant narrative that the cold and/or sedentary behavior explain the phenomenon.[22,26,31–33] To explore the hypothesis that SARS-CoV-2 infection could be a driver for some cases of PAP, we analyzed clinical samples from affected patients with PAP to profile the local immune response and screen for SARS-CoV-2 gene transcripts within lesions. Mechanistic feasibility was explored through a low-inoculum SARS-CoV-2 infection in the golden hamster model, which has been demonstrated to phenocopy human COVID-19 infection.[11,34–37]

RESULTS

Patients

In the USA, 54 patients were enrolled across four waves of the SARS-CoV-2 pandemic in Wisconsin, USA, from April 2020 to January 2022. Of these, 11 patients consented to biopsy of affected skin. In Europe, 11 patients consented to biopsies of affected skin which were used for validation of the *in situ* hybridization analysis from the Wisconsin, USA, cohort (Figure 1A). In the Wisconsin cohort, the incidence of PAP closely aligned with the time of peaking COVID-19 infection rates in Wisconsin (Figure 1B) and was proportional to an ambient temperature in Madison, Wisconsin, $\leq 9°C$ (Figure 1B). Thermal photography of patients affirmed an association with cold, revealing an alignment of the PAP lesional distribution with the coolest portions of the toes and fingers (Figure 1C).

An adaptive immune response is absent in patients with PAP

Antibody testing from both the US and European cohorts was consistent with the previous literature showing low rates of seroconversion (Table 1; Figure S1A). Control testing was overwhelmingly negative, reflecting sampling in the first few months of the pandemic when vaccines were unavailable (Figure S1A). Two patients in the Wisconsin cohort who tested positive for anti-nucleocapsid antibodies were total spike antibody negative, and subsequent testing for nucleocapsid within 8 weeks was negative. In the Wisconsin cohort ($n = 54$), the percentage of spike-specific T cells was not elevated in PAP patients compared to age- and sex-matched controls (Figures S1B–S1E). Collectively, these data demonstrate a lack of SARS-CoV-2-specific T cell and B cell immunity in affected PAP subjects, consistent with the previous literature.

Frequent plasmacytoid dendritic cells produce MxA near activated $CD3^+$T cells within PAP lesions

To investigate the local immune response in PAP, immunophenotyping was performed on the 11 affected Wisconsin, USA, biopsy samples, along with control samples (pre-2019 autopsy skin [$n = 4$] and pre-2019 histologically confirmed pernio [$n = 5$]) that had no logical possibility of exposure history to SARS-CoV-2 virus. In PAP sections, cellular infiltrates were distributed both deeply, around eccrine glands, and superficially, just below the epidermis. To investigate if an IFN-I response was detectable in affected skin, all samples were stained for Myxovirus resistance protein A (MxA), a downstream product of the IFN-I signaling cascade that serves as a surrogate marker of IFN-I signaling. Imaging and quantitation demonstrated significantly higher expression of MxA in PAP compared to pre-2019 autopsy skin, but pre-2019 pernio and PAP were statistically similar (Figure 2A). In addition, local immune cells and activation markers were stained in PAP and control tissues. Plasmacytoid dendritic cells (pDCs), an expected source of IFN-I, were evaluated using $CD303^+$ staining and were mainly found in the deep dermis. Cell numbers were quantitated, and comparison revealed a statistically significant elevation of pDCs relative to autopsy control skin, which was not statistically different from pre-2019 pernio control sections (Figure 2B).

Along with pDCs, PAP tissue had variable numbers of $CD3^+$ T lymphocytes (Figure 2C), and elevated expression of Type II IFN, interferon gamma (IFNγ, Figure 2D). Increased expression of human leukocyte antigen-DR isotype (HLA-DR), a key surface molecule expressed by antigen-presenting cells (APCs) and activated T cells, was also observed in PAP patients and pre-2019 pernio patients compared with pre-2019 normal skin (Figure 2E). Interestingly, few T cells expressed cytoplasmic MxA (Figure 2F), suggesting that these T cells were not responding directly to IFN-I and likely represented a cell population that was subsequently recruited following other immune cells such as the pDCs. Detailed microscopic analysis identified both activated T cells ($HLA\text{-}DR^+CD3^+$) and T cells in close proximity to $HLA\text{-}DR^+$ antigen presentign cells (APCs ($CD3^-$)), possibly marking immunologic synapses (Figures 2G and 2H). Overall, within this PAP cohort, there was clear and consistent local production of IFNs within a cellular milieu enriched in pDCs and $CD3^+$ T cells. The immune response was not statistically different in PAP and pre-2019 pernio specimens.

SARS-CoV-2 RNA is present in ~25% (6/22) of PAP lesions measured in 2 cohorts

Given the robust local IFN response detected in the Wisconsin PAP lesions, we next screened for the presence of SARS-CoV-2 RNA in PAP biopsies from both the cohorts ($n = 11$ from the Wisconsin, USA, and $n = 11$ from Switzerland) using RNAscope *in situ* hybridization. All cases tested were during patients' first presentation of PAP. SARS-CoV-2 S RNA was definitively and repeatably detected in 18% (2/11) of Wisconsin, USA, cases and subsequently in 36% (4/11) of Swiss cases (Figures 3A and 3B; Figure S2), with sparse distribution in the tissue. In an additional Wisconsin, USA, case, considered inconclusive, clustered sparse chromogenic dots were identified in multiple sections of the deep dermis near eccrine glands, but this was ultimately excluded when RNA was not clearly detected in a final replicate section. To ensure accuracy in the data, the total number of anatomically site-matched negative controls exceeded the number of PAP ($n = 22$) cases and included pre-2019 pernio ($n = 21$) and pre-2019 acral psoriasis ($n = 12$) biopsies. None of these negative controls (total $n = 33$) harbored detectable SARS-CoV-2 viral S sgRNA (Figures 3D and 3E). Positive controls included postmortem COVID-infected lung tissue (Figure 3C), which, as expected, contained frequent detectable SARS-CoV-2 viral RNA and was included in all sets of slides assayed. Additionally, positive (human peptidyl-prolyl isomerase B; Hs-PPIB) and negative (dihydrodipicolinate gene of *Bacilis subtilis*, DapB) control probes were used on all tissues to confirm assay validity and sample quality (Figures 3F–3M; Figure S2). All positive cases with RNA (Wisconsin $n = 2$; Swiss $n = 4$) were scored

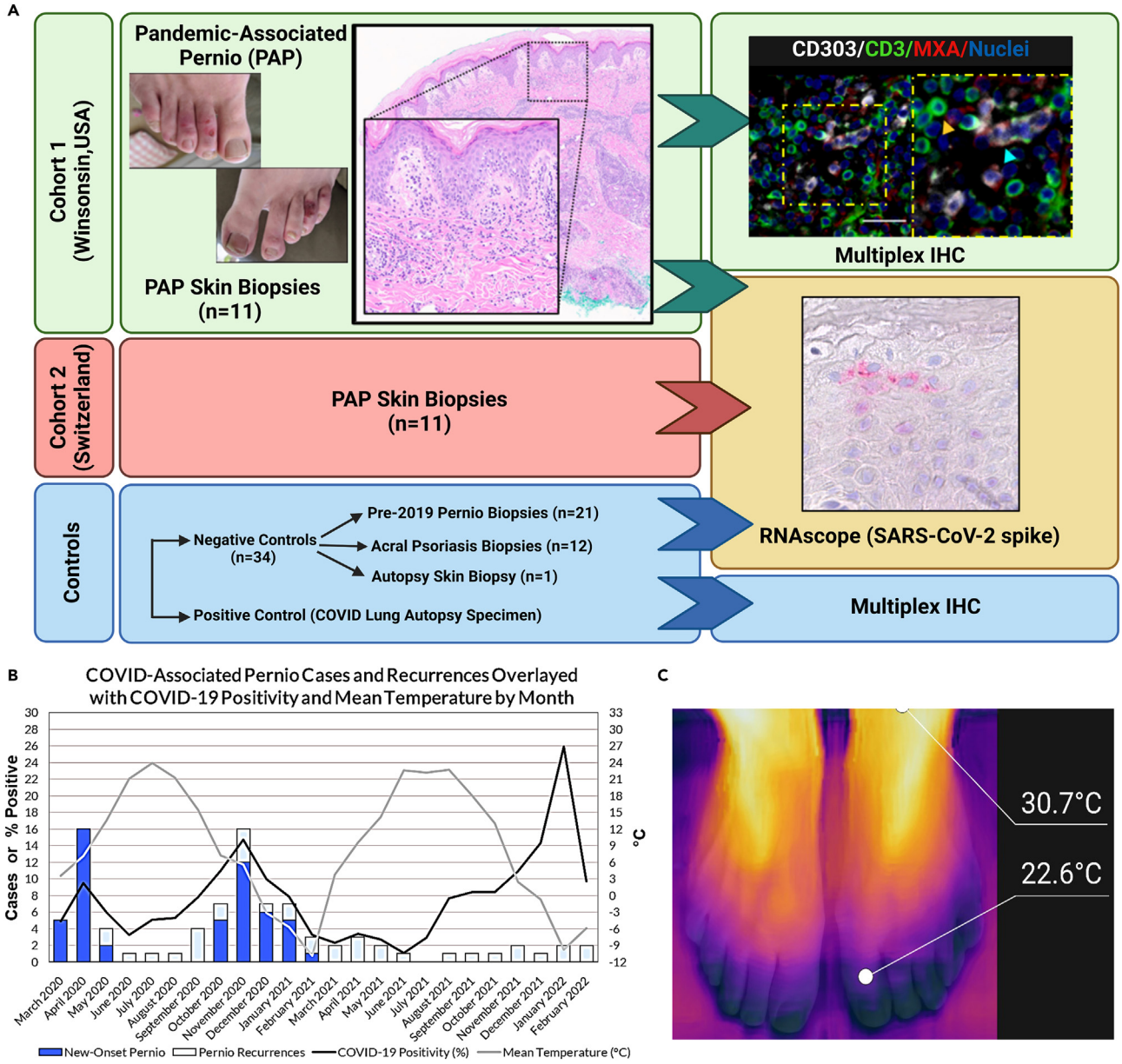

Figure 1. Clinical and histologic features of COVID-associated pernio

(A) Workflow of the study from Wisconsin, USA, and Switzerland cohorts along with classic findings of PAP including violaceous erythema, edema, vesiculation, ulceration, and a focused superficial and deep lymphocytic infiltration on H&E-stained tissue sections.

(B) Modified from Ng et al., BJD 2022,[38] to represent the Wisconsin cohort in the current investigation: Madison, Wisconsin, PAP cases and recurrences overlayed with COVID-19 positivity and mean temperature by month.

(C) Thermal photography image from an affected patient in Wisconsin: pernio lesions presented in the coldest areas of acral skin (in blue).

with high levels of inflammation by a pathologist (Figure 3N). All low inflammation cases were negative by RNAscope. Both Wisconsin cases demonstrated robust IFN-I activation with pDC infiltration on multiplex immunohistochemistry. Among patients with RNA positivity in the tissue, all patients in both the cohorts were SARS-CoV-2 PCR negative. One Swiss patient demonstrated IgG seroconversion, and the other three positive patients were negative by serology.

Hamster model demonstrates dissemination of viral RNA

To explore the mechanistic feasibility of SARS-CoV-2 viral material reaching acral sites in the setting of nasopharyngeal infection, we leveraged the golden hamster model (*M. auratus*),[11,34,35,39,40] which phenocopies the host response to SARS-CoV-2 in humans.[35] This model

Table 1. Clinical demographics of subjects with peripheral blood and skin biopsy studies in Wisconsin, USA, and Switzerland

Peripheral blood			Skin biopsy	
	Wisconsin, USA		Wisconsin, USA	Switzerland
	Pandemic-associated pernio (*n*= 54)	Healthy controls (*n*= 24)	Pandemic-associated pernio (*n*= 11)	Pandemic-associated pernio (*n*= 11)
Demographics				
Median age in years (range)	16 (2–59)	17 (9–34)	21.8 (12–59)	25 (16–44)
Sex (n, %)				
Female	27 (50%)	15 (63%)	6/11 (55%)	6/11 (55%)
Male	27 (50%)	9 (37%)	5/11 (45%)	5/11 (45%)
SARS-CoV-2 exposure history				
Suspected or confirmed SARS-CoV-2 exposure (n, %)	15 (28%)	–	4/11 (36%)	8/11 (62%)
Confirmed SARS-CoV-2 infection (nasopharyngeal SARS-CoV-2 PCR positive, n, %)	2/41 (5%)	–	0	2/11 (18%)
Peripheral Blood				
Time to presentation blood draw from symptom onset (weeks)	4 weeks (median 28 days)	–	7 weeks (4–8), drawn in 4/11 patients	5 weeks (1–12)
Total spike antibody IgG, IgM, IgA (n, %)	2/50 (4%)	0/24 (0%)	1/11 (9%)	–
Nucleocapsid IgG antibody (n, %)	2/39 (5%)	–	1/11 (9%)	3/11 (27%)
Skin biopsy				
Time to biopsy from symptom onset (median, weeks)	–	–	5 (2–12)	5 (1–12)
Localized inflammatory responses				
High inflammation	–		9/11 (82%)	7/11 (64%)
Low inflammation	–		2/11 (18%)	4/11 (36%)
Multiplex IHC with high type 1 IFN			11/11	–
RNAscope with SARS-CoV-2 RNA positivity			2/11, all with high inflammation	4/11, all with high inflammation

employs low-dose intranasal SARS-CoV-2 inoculation to initiate an infection with similar viral tissue tropism as that observed in humans. The model notably reproduces an array of symptomologies seen in human COVID-19 patients including SARS-CoV-2-specific anosmia,[34] sensory abnormalities,[41] and lung pathology.[11] Here, the hamster model was used to test for dissemination of viral material to acral tissues and to evaluate the local IFN-I response. Of note, an animal model of pernio does not exist, and this model does not recapitulate clinical pernio.

Following intranasal inoculation of hamsters, viral RNA was detected in lung tissue as early as 1 day post-infection (dpi). After this point, lung viral RNA levels peaked at 3 dpi and then rapidly dropped to near-background levels between 7 and 10 dpi (Figure 4A), consistent with previously published data.[11,34] Quantitative reverse-transcription PCR (RT-qPCR) for *Isg15* indicated an IFN-I response in the lung which correlated to viral RNA levels over time (Figure 4B). In longitudinally collected hamster toe tissues, RT-qPCR assays demonstrated dissemination of viral RNA to toes following intranasal inoculation with SARS-CoV-2 (Figure 4C). Sub-genomic N protein (sgN) RNA levels were first detectable at 1 dpi and were measurable in all toe tissues by 3 dpi. RNA levels appeared to decline to background levels between 5–7 dpi (Figure 4C). Similarly, RT-qPCR for *Isg15* in toe tissues also demonstrated an active IFN response that peaked at 3 dpi and appeared to track with the presence of viral RNA in the tissue (Figure 4D).

When RT-qPCR values for Isg15 levels in the toes were plotted against viral RNA values, (Figure S3A) linear regression on the resulting graph showed a significant positive correlation ($p < 0.0001$; slope = 1734; $r^2 = 0.5917$) between viral RNA levels and the local IFN-I response denoted by Isg15 induction in these tissues. Importantly, *Isg15* levels in the toes did not mirror those seen in the lungs of the same hamsters, as lung *Isg15* reached a peak relative expression at 5 dpi in the lungs while *Isg15* levels in the toe had declined significantly from their 3 dpi peak at this same time point (Figures 4B and 4D).

To assess if the presence of SARS-CoV-2 transcripts in the toes resulted from replicating viral infection, homogenized toe tissue harvested at the time of peak detectable subgenomic RNA (sgRNA) signal, 3dpi, was assessed by plaque assay (Figure 4E) and yielded no plaques, demonstrating that, in standard intranasal inoculation conditions, replicating virions could not be detected in acral sites.[42] western blot analysis of toe homogenate was also negative for the presence of SARS-CoV-2 nucleocapsid protein (Figure S3B). As IFN-I induction requires the

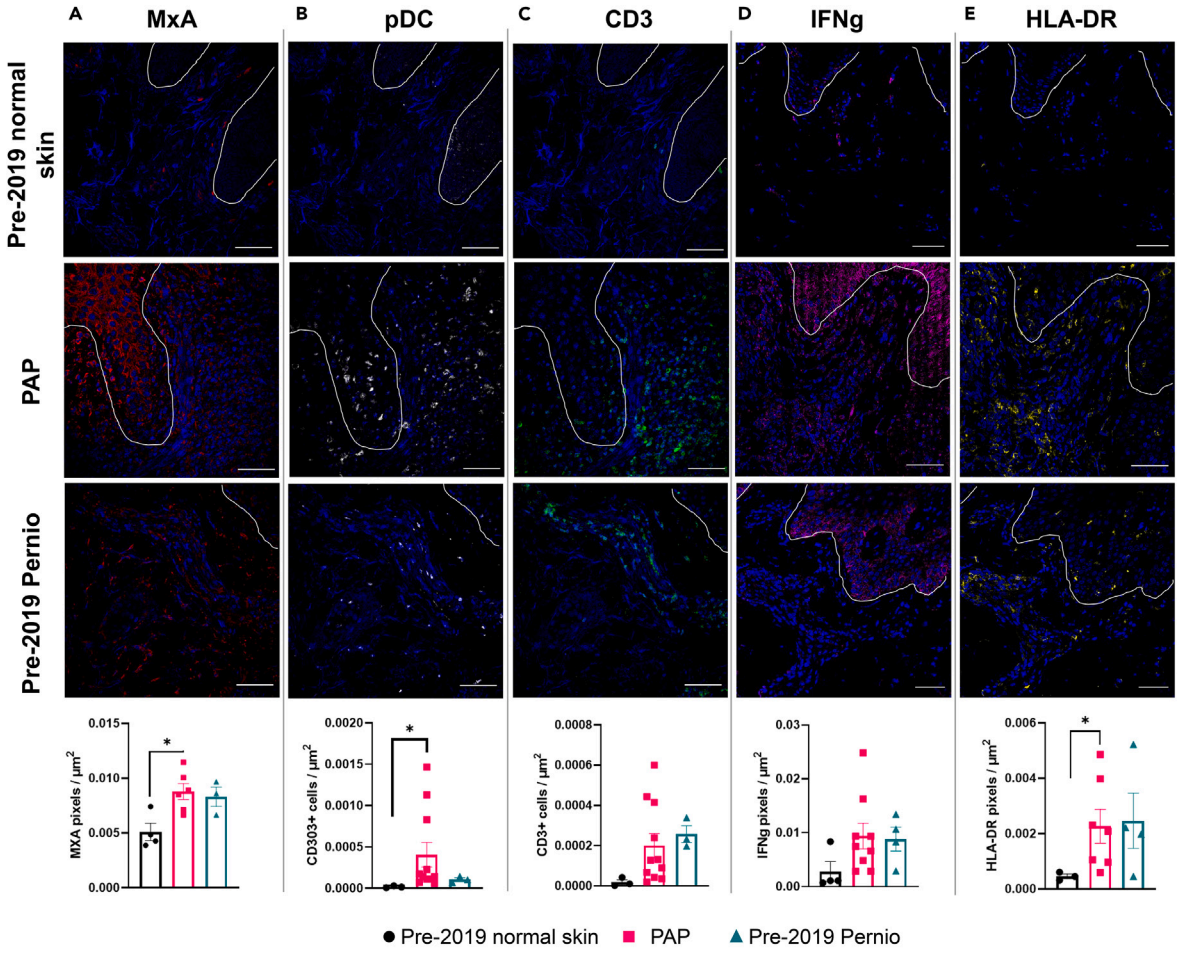
A MxA
B pDC
C CD3
D IFNg
E HLA-DR
Pre-2019 normal skin
PAP
Pre-2019 Pernio
MXA pixels / µm²
CD303+ cells / µm²
CD3+ cells / µm²
IFNg pixels / µm²
HLA-DR pixels / µm²
Pre-2019 normal skin
PAP
Pre-2019 Pernio

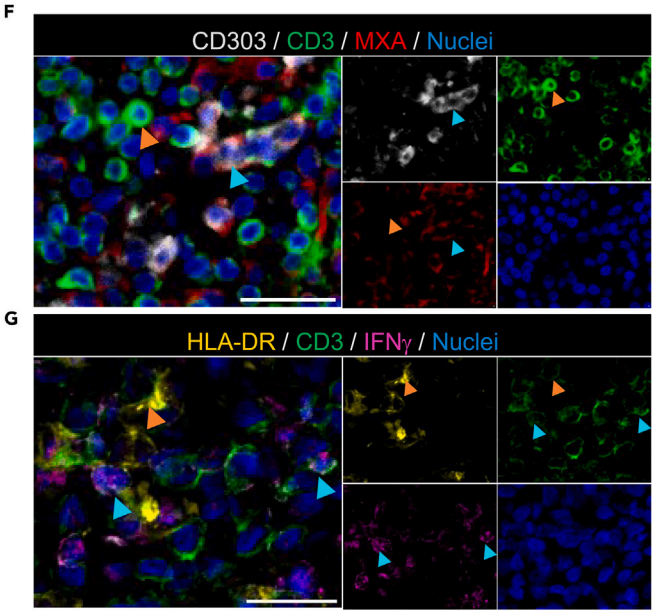
F
CD303 / CD3 / MXA / Nuclei
G
HLA-DR / CD3 / IFNγ / Nuclei

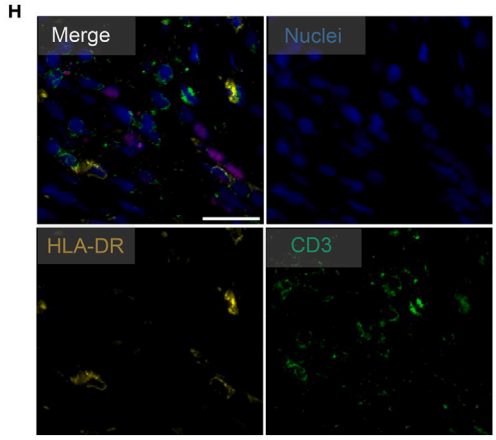
H
Merge
Nuclei
HLA-DR
CD3

Figure 2. Anti-viral immune response profile in COVID-associated pernio

Representative confocal images and summary quantification of MxA (A; in red), CD303 (B; in gray), CD3 (C; in green), IFNγ (D; in magenta), and HLA-DR (E; in yellow) in representative negative control pre-2019 normal skin (first row, n = 3–4), pandemic-associated pernio (PAP; second row, n = 6–11), and pre-2019 pernio lesions (third row, n = 3–4). White dotted lines indicate the dermal-epidermal junction. Atto-465p (A, B, and C) and DAPI (D and E) were used to counterstain nuclei. $CD3^+$T cells and $CD303^+$pDCs were counted in the entire biopsy section for each patient; positive pixel quantification was performed for MxA, IFNγ, and HLA-DR. Numbers were normalized by the total area of the tissue (in μm^2). Magnification, ×40; scale bar, 50 μm. Bars in graph represent mean ± SEM. *$p < 0.05$ in Kruskal-Wallis test with Dunn's correction for multiple comparisons.

(F) Dense immune cell infiltrate consisting primarily of T cells (green) and pDCs (gray) in patients with PAP. Expression of MxA (red) by pDCs (cyan arrowhead), but rarely by T cells (orange arrowhead). Nuclei were stained with Atto-465p.

(G) Presence of activated T cells in PAP tissue. Orange arrowhead shows the close proximity between HLA-DR-expressing cells (yellow) and CD3 T cells(green), indicating a possible synapse. Cyan arrowheads show activated T cells expressing IFNγ (magenta). Nuclei were stained with DAPI.

(H) Both T cells (green) establishing communication with HLA-DR+ cells (yellow; white arrowhead) and T cells expressing HLA-DR are present in PAP lesions. Magnification, ×40; scale bar, 50 μm.

direct presence of pathogen associated molecular patterns (PAMPs) these data suggest that viral RNA, viral debris, or the host response, but not replicating virus or active infection, underlie the IFN-I signature observed in distal tissues.

To better understand the longitudinal transcriptional programs active in SARS-CoV-2-infected hamster toes, RNA sequencing (RNA-seq) was performed on homogenized toe tissues at both early (3 dpi) and late (30 dpi) time points following inoculation ($n = 4$ per infection and time point group) (Figures 4F and 4G). Initial analysis of viral reads in RNA-seq data demonstrated detection of SARS-CoV-2 transcripts in toe tissues at 3dpi, confirming earlier qPCR data (Figures 4C and S3C). Differential expression analysis revealed induction of >200 host genes in the toes of hamsters 3 dpi as compared to mock-treated animals (Figure S3D; Table S1). Gene set enrichment analysis identified significant induction of the canonical IFN-I pathway in toes, further confirming prior qPCR *ISG15* data (Figure 4F). Comparison of the IFN-I response between the toes and the lung during acute SARS-CoV-2 infection showed that, while both tissue sites demonstrated a robust IFN-I response at 3dpi, the magnitude of this transcriptional signature was higher in the lung, the site of viral replication. This was apparent both through the breadth of ISGs and the magnitude of pathway induction in infected lungs compared to infected toes (Figure 4G; Table S1). Notably, at 30 dpi, both lung and toe tissues returned to a baseline IFN-I state (Figures S3E and S3F; Table S2). Together, these results indicate that systemic IFN-I signaling likely correlates with infectious burden, but that viral RNA may trigger localized inflammation and IFN-I responses in distal tissues including toes.

DISCUSSION

The increased incidence of pernio early during the COVID-19 pandemic has remained a pervasive enigma in dermatology, in part because patients overwhelmingly tested negative for SARS-CoV-2 exposure. In this work, we identify evidence that SARS-CoV-2 infection results in the systemic distribution of inflammatory material "from your nose to your toes" in both human samples and a SARS-CoV-2-infected small animal model. In patient cohorts collected simultaneously on two continents, 18%–36% (~25%; 6/22) of patients with biopsied pernio harbored detectable S gene RNA confirming the presence of SARS-CoV-2 sub-genomic RNA at acral sites. Importantly, no patients with sparse SARS-CoV-2 viral RNA in skin were nasopharyngeal PCR positive, and only one patient harboring RNA in skin developed evidence of seroconversion. In the aggregate, these data confirm that lesional site SARS-CoV-2 RNA, when present in PAP, is truly sparse, is difficult to detect, and does not represent a reservoir of active viral replication. As highlighted by other studies, this study corroborates that SARS-CoV-2 viral debris can persist in non-respiratory tissues, perhaps due to tissue-specific differences in the magnitude of the immune response and its efficiency in RNA clearance.[43]

In the Wisconsin cohort, robust local IFN expression was accompanied by pDC activation that persisted well after clearance of viral RNA. Evidence presented here does not definitively link the presence of spike RNA in these lesions with pDC activation and the robust local immune response. However, the evidence suggests that these responses are likely linked. Importantly, pre-2019 pernio cases looked identical to PAP on immunohistochemistry, suggesting that the local immune response in all forms of pernio are similar, despite the absence of SARS-CoV-2 prior to 2019. The cause of pre-pandemic pernio is beyond the scope of this investigation, but additional triggers, including potentially disseminated viral particles or debris from a distal infection, might contribute. Because accumulating evidence suggests that other IFN-I-mediated autoimmune disorders, including dermatomyositis and lupus, can be triggered by preceding viral infection, we hypothesize that some cases of pernio, including prior to the onset of the SARS-CoV-2 pandemic, may have been triggered by other viral exposures.

To better understand the driver of pernio given the limitations posed by these rare patient samples, we leveraged the golden hamster as a surrogate for this biology. In this model, nasopharyngeal SARS-CoV-2 RNA could be readily detected in the toes and, in turn, produced a wide-ranging IFN-I response. Although toe tissues harbored detectable viral RNA, it was non-infectious, suggesting there is no active viral replication in the skin. Together, these pieces of evidence suggest that, during SARS-CoV-2 infection, cells or apoptotic bodies containing viral material can enter the circulation and be deposited in distal tissues such as the toes, where they may induce an interferon response.

There was no evidence of adaptive immunity in this cohort, consistent with previous reports.[26,44] The persistent local IFN-I response in skin, coupled to previous reports demonstrating an early and transient IFN-I systemic host response,[29,30,44] challenges the conventional dogma that a strong innate immune response should give rise to an effective adaptive response. In cases with evidence of SARS-CoV-2 S RNA in tissue, we postulate that low rates of peripheral adaptive immunity could reflect the efficiency of an early and transient naso-respiratory innate immune response to clear the virus from the nasopharynx,[10] obviating a robust adaptive response and creating an abortive, seronegative

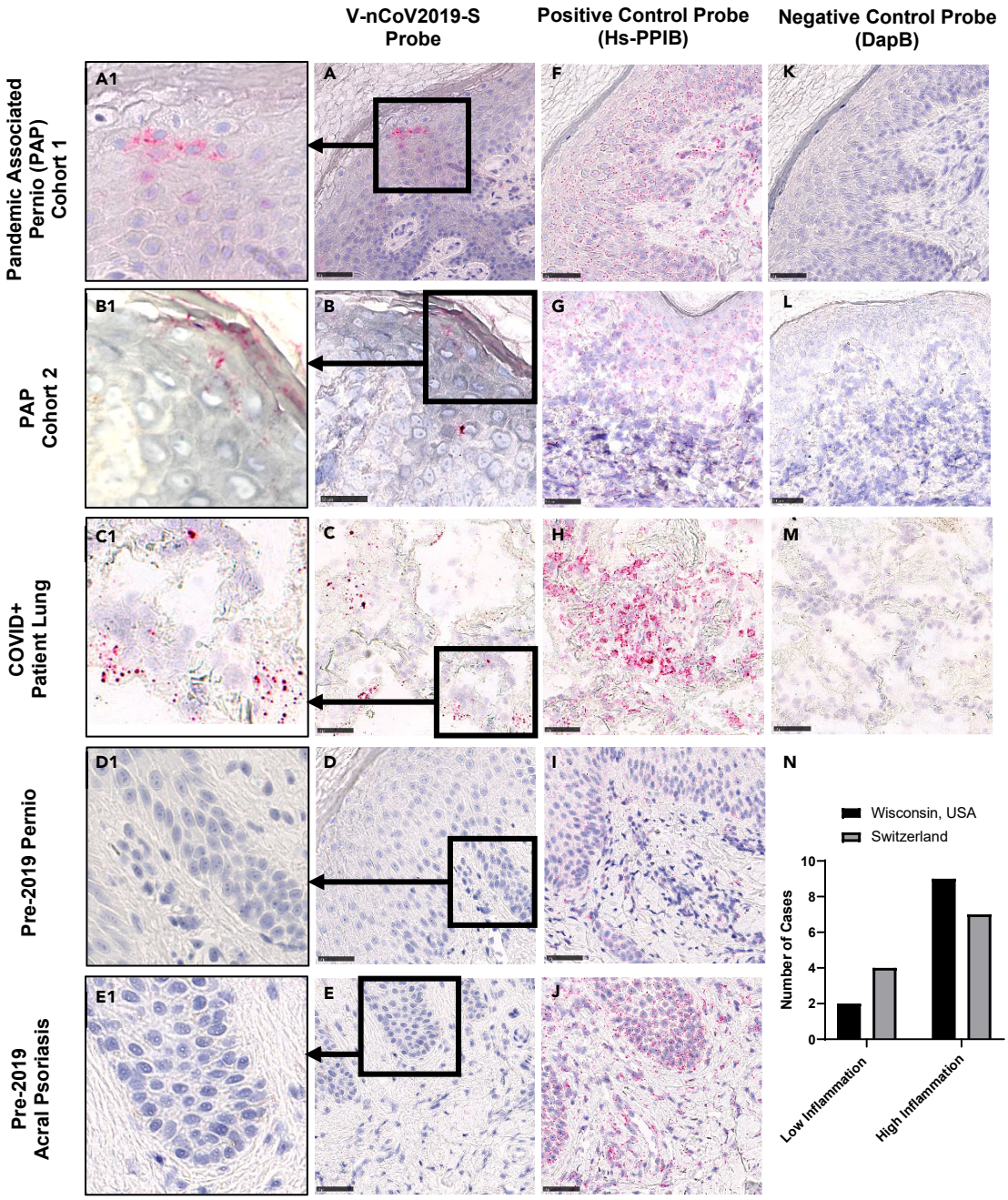

Figure 3. SARS-CoV-2 RNA presence in representative PAP lesions

RNAscope *in situ* hybridization was used to detect the presence of SARS-CoV-2 viral RNA in formalin-fixed, paraffin-embedded (FFPE) tissue sections from representative PAP from Wisconsin, USA, patient cohort 1 (A) and PAP from Switzerland cohort 2 (B); autopsy lung tissue from a COVID-19 patient was used as a SARS-CoV-2 viral RNA probe positive control (C); pre-2019 pernio lesions (D) and pre-2019 acral psoriasis lesions were used as negative controls (E). 60x high-resolution images are shown in A1–E1, respectively. A probe for the housekeeping gene *PPIB* was used as a positive assay control (F–J), negative-control target probe *DapB* (K–M). Magnification x20. Scale bar, 50 μm.

(N) Bar Graph showing the low and high inflammation score distribution of cases in Wisconsin, USA, and Switzerland cohorts.

See also Figure S2.

infection, with few extracutaneous manifestations. This is supported by other SARS-CoV-2 studies demonstrating that younger patients with lower nasopharyngeal loads commonly fail to seroconvert.[45] The absence of adaptive immunity could also suggest a lower inoculum of infection, which could not be assessed in this investigation.

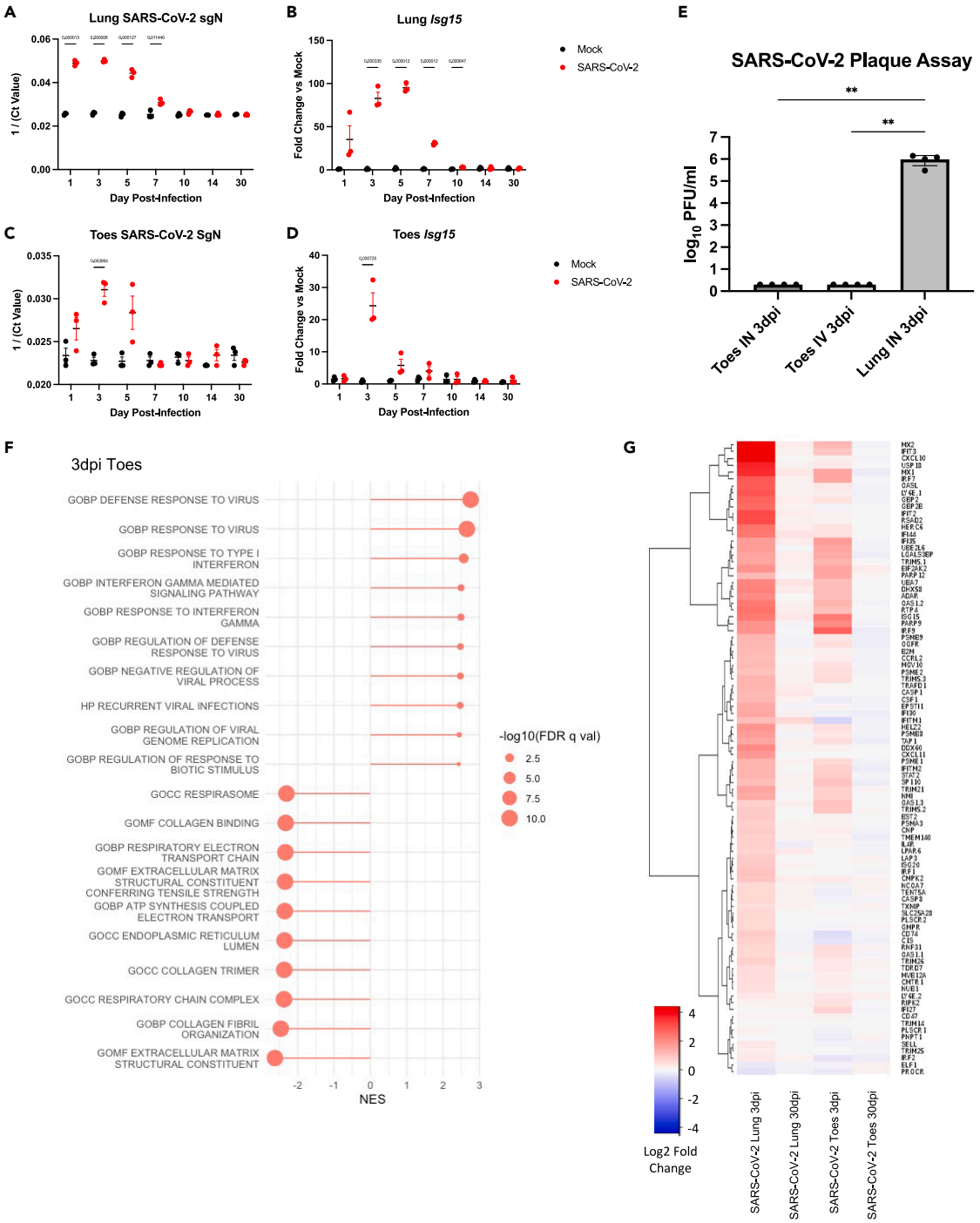

Figure 4. Golden hamsters were intranasally treated with SARS-CoV-2 or PBS (mock)

Lung and toe tissues from SARS-CoV-2- and mock-treated hamsters were longitudinally harvested at days 1, 3, 5, 7, 10, 14, and 30 post-infection (n = 3 per condition per time point).

(A and B) Lung tissues were then assessed for the presence of (A) SARS-CoV-2 sgN and (B) *Isg15* transcripts via RT-qPCR.

(C and D) Toe tissues were also assessed for (C) sgN and (D) *Isg15* presence via RT-qPCR. Significance was evaluated via multiple unpaired t tests performed using a two-stage step-up method to control the false discovery rate (FDR). FDR q-values less than 0.05 are displayed.

(E) Toes were harvested from 3dpi hamsters inoculated with SARS-CoV-2 via either intranasal (IN) or intravenous (IV) routes and assessed for the presence of infectious virus via plaque assay. 3 dpi lung samples from SARS-CoV-2-infected hamsters were included as a positive control (n = 4 per condition). Significance was calculated using an ordinary one-way ANOVA with Tukey's multiple comparisons test. $^{**}p < 0.01$.

Figure 4. *Continued*

(F and G) Toe and lung tissues were harvested at 3 days post-infection (dpi) and 30 dpi and transcriptionally profiled using RNA sequencing. SARS-CoV-2- and mock-treated datasets were compared in differential expression analysis (n = 2–4 for respective time point and infection groups). Toe differential expression data of 3dpi harvested toes was in turn analyzed using gene set enrichment analysis (GSEA) for enrichment of ontology-related gene sets (MSigDB Gene Set C5). Top enrichments from these analyses are represented in (F) as a lollipop chart, with magnitude of the stalk representative of normalized enrichment score (NES) and dot size scaled to significance.

(G) RNA sequencing data for SARS-CoV-2-infected toes and lungs at 3 and 30 dpi were compared to analogous mock-treated tissues using differential expression analysis. Log2(fold change) of type I interferon-stimulated genes are presented here as a heatmap.

See also Figure S3.

These findings have potential implications for understanding the role of SARS-CoV-2-mediated IFN-I activation in skin. Cutaneous deposition of type I interferons are the hallmark of a range of autoimmune skin disorders including cutaneous lupus, dermatomyositis, morphea, vitiligo, and alopecia areata, many of which are speculated to have a viral trigger.[46–59] Viral and other causes of cell death including trauma, medications, UV radiation, and cold are speculated to induce cell death and lead to the release of nuclear fragments and induce local IFN-I production.[50,51] In this regard, it is tempting to speculate that sgRNA deposition might be enhanced in environments of cold temperatures, where circulation slows to allow more time for such material to exit the blood. Cutaneous ischemia/damage, in some cases coupled to the presence of viral RNA waiting to be recognized by PAMPs, could favor a local IFN-I signature on rewarming, with recruitment of pDCs and subsequently lymphocytes that results in a durable and often recurrent cutaneous immune response. Understanding potential mechanisms by which SARS-CoV-2 evades immune detection during cold temperatures and other conditions is beyond the scope of the current report but is critical to guide future therapeutic approaches to this virus and autoimmune skin disorders.

Limitations of the study

By its nature, there are significant limitations to this work, including lack of mechanistic data in the human samples. Pre-2019 pernio biopsies demonstrated a local IFN-1 response that was not different from pandemic-era biopsies. We were unable to interrogate a host of additional viral infections via *in situ* hybridization and cannot rule out that other circulating viral infections played a role in triggering the phenotype. This work also does not exclude other potential triggers for pernio, including but not limited to cold, trauma, or perhaps other viral infections. This work is also limited by the absence of functional studies in a pernio-specific animal model. In the hamster model, viral RNA was cleared within 7 days, suggesting that the presence of viral RNA in acral tissues is indeed transient and further underscoring the difficulty of detecting RNA in human samples, as most patients presented weeks after pernio onset. Finally, pernio incidence has waned with newer SARS-CoV-2 variants, restricting more detailed additional studies. Newer variants appear more confined to the upper respiratory tract, which may translate to less cellular debris in the circulation, although the mechanism producing waning incidence is uncertain.

STAR★METHODS

Detailed methods are provided in the online version of this paper and include the following:

- KEY RESOURCES TABLE
- RESOURCE AVAILABILITY
  - Lead contact
  - Materials availability
  - Data and code availability
- EXPERIMENTAL MODEL AND STUDY PARTICIPANT DETAILS
  - Patients
- METHOD DETAILS
  - Activation induced marker (AIM) assay
  - Tissue analysis
  - *In situ* hybridization (RNAscope)
  - Hamster model
  - Viruses and plaque assays
  - RNA extraction and quantitative reverse transcription polymerase chain reaction
  - RNA sequencing and analysis
  - Western blot
  - PBMC isolation
  - Activation induced marker (AIM) assay
  - Immunohistochemistry
  - *In situ* hybridization (RNAscope)
- QUANTIFICATION AND STATISTICAL ANALYSIS
- ADDITIONAL RESOURCES

SUPPLEMENTAL INFORMATION

Supplemental information can be found online at https://doi.org/10.1016/j.isci.2024.110525.

ACKNOWLEDGMENTS

The authors extend gratitude to the patients and their families for their critical participation in this research. This work was funded by the Wisconsin Partnership Program 2020 Strategic COVID-19 Grant, the Intramural Program of the National Institute of Dental and Craniofacial Research, National Institutes of Health (ZIA DE000747 Mays), and the Intramural Program of the National Institute of Arthritis and Musculoskeletal and Skin Diseases, NIH. Imaging support came from NIDCR Imaging Core (ZIC DE00075), with specific thanks to Dr. Andrew Doyle for his technical expertise. SARS-CoV-2-specific T cell studies were funded by 2R24OD017850-05, *High-throughput identification of common CD8$^+$ T cell responses to SIV and M. tuberculosis in rhesus macaques*. We would also like to acknowledge the NYU Langone Genome Technology Center for their assistance in conducting the RNA sequencing of hamster tissues. We also thank Heather Neils, Ellen Bruhn, and Marcos Lares for regulatory and research support and Dr. Bridget Shields for patient recruitment.

AUTHOR CONTRIBUTIONS

Conceptualization: L.M.A., A.C.C.-d.-S., J.F., H.E.B., D.H.O., E.W.C., B.A.D., B.t., A.M.S., and J.W.M.. Investigation: A. Ng, J.J.M., R.S., C.H.K., A.J., O.R.S., J.T.N., A. Nihal, G.L., M.K., L.C., J.M.T., M.A.H., H.E.B., E.G.B., A.Y., F.S., M.G., and A.M.S. Formal analysis: L.M.A., A.C.C.-d.-S., J.F., H.E.B., D.H.O., R.S., E.W.C., B.A.D., B.t., A.M.S., and J.W.M.. Writing – original draft: L.M.A., A.C.C.-d.-S., J.F., R.S., H.E.B., E.W.C., J.-L.C., D.H.O., B.A.D., B.t., A.M.S., and J.W.M.. Writing – review and editing: all authors.

DECLARATION OF INTERESTS

The authors declare no competing interests.

Received: December 27, 2023
Revised: May 31, 2024
Accepted: July 12, 2024
Published: July 17, 2024

REFERENCES

1. Zhang, Q., Bastard, P., Liu, Z., Le Pen, J., Moncada-Velez, M., Chen, J., Ogishi, M., Sabli, I.K.D., Hodeib, S., Korol, C., et al. (2020). Inborn errors of type I IFN immunity in patients with life-threatening COVID-19. Science *370*, eabd4570. https://doi.org/10.1126/science.abd4570.
2. Bastard, P., Gervais, A., Le Voyer, T., Rosain, J., Philippot, Q., Manry, J., Michailidis, E., Hoffmann, H.H., Eto, S., Garcia-Prat, M., et al. (2021). Autoantibodies neutralizing type I IFNs are present in ~4% of uninfected individuals over 70 years old and account for ~20% of COVID-$_{19}$ deaths. Sci. Immunol. *6*, eabl4340. https://doi.org/10.1126/sciimmunol.abl4340.
3. Bastard, P., Rosen, L.B., Zhang, Q., Michailidis, E., Hoffmann, H.H., Zhang, Y., Dorgham, K., Philippot, Q., Rosain, J., Beziat, V., et al. (2020). Autoantibodies against type I IFNs in patients with life-threatening COVID-19. Science *370*, eabd4585. https://doi.org/10.1126/science.abd4585.
4. Asano, T., Boisson, B., Onodi, F., Matuozzo, D., Moncada-Velez, M., Maglorius Renkilaraj, M.R.L., Zhang, P., Meertens, L., Bolze, A., Materna, M., et al. (2021). X-linked recessive TLR7 deficiency in ~1% of men under 60 years old with life-threatening COVID-19. Sci. Immunol. *6*, eabl4348. https://doi.org/10.1126/sciimmunol.abl4348.
5. Matuozzo, D., Talouarn, E., Marchal, A., Zhang, P., Manry, J., Seeleuthner, Y., Zhang, Y., Bolze, A., Chaldebas, M., Milisavljevic, B., et al. (2023). Rare predicted loss-of-function variants of type I IFN immunity genes are associated with life-threatening COVID-19. Genome Med. *15*, 22. https://doi.org/10.1186/s13073-023-01173-8.
6. Zhang, Q., Matuozzo, D., Le Pen, J., Lee, D., Moens, L., Asano, T., Bohlen, J., Liu, Z., Moncada-Velez, M., Kendir-Demirkol, Y., et al. (2022). Recessive inborn errors of type I IFN immunity in children with COVID-19 pneumonia. J. Exp. Med. *219*, e20220131. https://doi.org/10.1084/jem.20220131.
7. Manry, J., Bastard, P., Gervais, A., Le Voyer, T., Rosain, J., Philippot, Q., Michailidis, E., Hoffmann, H.H., Eto, S., Garcia-Prat, M., et al. (2022). The risk of COVID-19 death is much greater and age dependent with type I IFN autoantibodies. Proc. Natl. Acad. Sci. USA *119*, e2200413119. https://doi.org/10.1073/pnas.2200413119.
8. Tovo, P.A., Garazzino, S., Daprà, V., Pruccoli, G., Calvi, C., Mignone, F., Alliaudi, C., Denina, M., Scolfaro, C., Zoppo, M., et al. (2021). COVID-19 in Children: Expressions of Type I/II/III Interferons, TRIM28, SETDB1, and Endogenous Retroviruses in Mild and Severe Cases. Int. J. Mol. Sci. *22*, 7481. https://doi.org/10.3390/ijms22147481.
9. Sacco, K., Castagnoli, R., Vakkilainen, S., Liu, C., Delmonte, O.M., Oguz, C., Kaplan, I.M., Alehashemi, S., Burbelo, P.D., Bhuyan, F., et al. (2022). Immunopathological signatures in multisystem inflammatory syndrome in children and pediatric COVID-19. Nat. Med. *28*, 1050–1062. https://doi.org/10.1038/s41591-022-01724-3.
10. Pierce, C.A., Sy, S., Galen, B., Goldstein, D.Y., Orner, E., Keller, M.J., Herold, K.C., and Herold, B.C. (2021). Natural mucosal barriers and COVID-19 in children. JCI Insight *6*, e148694. https://doi.org/10.1172/jci.insight.148694.
11. Hoagland, D.A., Møller, R., Uhl, S.A., Oishi, K., Frere, J., Golynker, I., Horiuchi, S., Panis, M., Blanco-Melo, D., Sachs, D., et al. (2021). Leveraging the antiviral type I interferon system as a first line of defense against SARS-CoV-2 pathogenicity. Immunity *54*, 557–570. https://doi.org/10.1016/j.immuni.2021.01.017.
12. Reis, G., Moreira Silva, E.A.S., Medeiros Silva, D.C., Thabane, L., Campos, V.H.S., Ferreira, T.S., Santos, C.V.Q., Nogueira, A.M.R., Almeida, A., Savassi, L.C.M., et al. (2023). Early Treatment with Pegylated Interferon Lambda for Covid-19. N. Engl. J. Med. *388*, 518–528. https://doi.org/10.1056/NEJMoa2209760.
13. Crow, Y.J., and Casanova, J.L. (2014). STING-associated vasculopathy with onset in infancy–a new interferonopathy. N. Engl. J. Med. *371*, 568–571. https://doi.org/10.1056/NEJMe1407246.
14. Crow, Y.J., Chase, D.S., Lowenstein Schmidt, J., Szynkiewicz, M., Forte, G.M., Gornall, H.L., Oojageer, A., Anderson, B., Pizzino, A., Helman, G., et al. (2015). Characterization of human disease phenotypes associated with mutations in TREX1, RNASEH2A, RNASEH2B, RNASEH2C, SAMHD1, ADAR, and IFIH1. Am. J. Med. Genet. *167A*, 296–312. https://doi.org/10.1002/ajmg.a.36887.
15. Ravenscroft, J.C., Suri, M., Rice, G.I., Szynkiewicz, M., and Crow, Y.J. (2011). Autosomal dominant inheritance of a heterozygous mutation in SAMHD1 causing familial chilblain lupus. Am. J. Med. Genet.

155A, 235–237. https://doi.org/10.1002/ajmg.a.33778.

16. Rice, G., Newman, W.G., Dean, J., Patrick, T., Parmar, R., Flintoff, K., Robins, P., Harvey, S., Hollis, T., O'Hara, A., et al. (2007). Heterozygous mutations in TREX1 cause familial chilblain lupus and dominant Aicardi-Goutieres syndrome. Am. J. Hum. Genet. *80*, 811–815. https://doi.org/10.1086/513443.
17. Freeman, E.E., McMahon, D.E., Lipoff, J.B., Rosenbach, M., Kovarik, C., Takeshita, J., French, L.E., Thiers, B.H., Hruza, G.J., and Fox, L.P.; American Academy of Dermatology Ad Hoc Task Force on COVID-19 (2020). Pernio-like skin lesions associated with COVID-19: A case series of 318 patients from 8 countries. J. Am. Acad. Dermatol. *83*, 486–492. https://doi.org/10.1016/j.jaad.2020.05.109.
18. Colonna, C., Genovese, G., Monzani, N.A., Picca, M., Boggio, F., Gianotti, R., and Marzano, A.V. (2020). Outbreak of chilblain-like acral lesions in children in the metropolitan area of Milan, Italy, during the COVID-19 pandemic. J. Am. Acad. Dermatol. *83*, 965–969. https://doi.org/10.1016/j.jaad.2020.06.019.
19. Andina, D., Noguera-Morel, L., Bascuas-Arribas, M., Gaitero-Tristan, J., Alonso-Cadenas, J.A., Escalada-Pellitero, S., Hernandez-Martin, A., de la Torre-Espi, M., Colmenero, I., and Torrelo, A. (2020). Chilblains in children in the setting of COVID-19 pandemic. Pediatr. Dermatol. *37*, 406–411. https://doi.org/10.1111/pde.14215.
20. Castelo-Soccio, L., Lara-Corrales, I., Paller, A.S., Bean, E., Rangu, S., Oboite, M., Flohr, C., Ahmad, R.C., Calberg, V., Gilliam, A., et al. (2021). Acral Changes in pediatric patients during COVID 19 pandemic: Registry report from the COVID 19 response task force of the society of pediatric dermatology (SPD) and pediatric dermatology research alliance (PeDRA). Pediatr. Dermatol. *38*, 364–370. https://doi.org/10.1111/pde.14566.
21. Cordoro, K.M., Reynolds, S.D., Wattier, R., and McCalmont, T.H. (2020). Clustered cases of acral perniosis: Clinical features, histopathology, and relationship to COVID-19. Pediatr. Dermatol. *37*, 419–423. https://doi.org/10.1111/pde.14227.
22. McCleskey, P.E., Zimmerman, B., Lieberman, A., Liu, L., Chen, C., Gorouhi, F., Jacobson, C.C., Lee, D.S., Sriram, A., Thornton, A., et al. (2021). Epidemiologic Analysis of Chilblains Cohorts Before and During the COVID-19 Pandemic. JAMA Dermatol. *157*, 947–953. https://doi.org/10.1001/jamadermatol.2021.2120.
23. Feito-Rodríguez, M., Mayor-Ibarguren, A., Camara-Hijon, C., Montero-Vega, D., Servera-Negre, G., Ruiz-Bravo, E., Nozal, P., Rodriguez-Peralto, J.L., Enguita, A.B., Bravo-Gallego, L.Y., et al. (2021). Chilblain-like lesions and COVID-19 infection: A prospective observational study at Spain's ground zero. J. Am. Acad. Dermatol. *84*, 507–509. https://doi.org/10.1016/j.jaad.2020.09.086.
24. Moghadam, P., Frumholtz, L., Jaume, L., De Masson, A., Jachiet, M., Begon, E., Sulimovic, L., Petit, A., Bachelez, H., Bagot, M., et al. (2021). Frequency of relapse and persistent cutaneous symptoms after a first episode of chilblain-like lesion during the COVID-19 pandemic. J. Eur. Acad. Dermatol. Venereol. *35*, e566–e568. https://doi.org/10.1111/jdv.17393.
25. Le Cleach, L., Dousset, L., Assier, H., Fourati, S., Barbarot, S., Boulard, C., Bourseau Quetier, C., Cambon, L., Cazanave, C., Colin, A., et al. (2020). Most chilblains observed during the COVID-19 outbreak occur in patients who are negative for COVID-19 on polymerase chain reaction and serology testing. Br. J. Dermatol. *183*, 866–874. https://doi.org/10.1111/bjd.19377.
26. Gehlhausen, J.R., Little, A.J., Ko, C.J., Emmenegger, M., Lucas, C., Wong, P., Klein, J., Lu, P., Mao, T., Jaycox, J., et al. (2022). Lack of association between pandemic chilblains and SARS-CoV-2 infection. Proc. Natl. Acad. Sci. USA *119*, e2122090119. https://doi.org/10.1073/pnas.2122090119.
27. Hubiche, T., Le Duff, F., Chiaverini, C., Giordanengo, V., and Passeron, T. (2021). Negative SARS-CoV-2 PCR in patients with chilblain-like lesions. Lancet Infect. Dis. *21*, 315–316. https://doi.org/10.1016/S1473-3099(20)30518-1.
28. Frumholtz, L., Bouaziz, J.D., Battistella, M., Hadjadj, J., Chocron, R., Bengoufa, D., Le Buanec, H., Barnabei, L., Meynier, S., Schwartz, O., et al. (2021). Type I interferon response and vascular alteration in chilblain-like lesions during the COVID-19 outbreak. Br. J. Dermatol. *185*, 1176–1185. https://doi.org/10.1111/bjd.20707.
29. Hubiche, T., Cardot-Leccia, N., Le Duff, F., Seitz-Polski, B., Giordana, P., Chiaverini, C., Giordanengo, V., Gonfrier, G., Raimondi, V., Bausset, O., et al. (2021). Clinical, Laboratory, and Interferon-Alpha Response Characteristics of Patients With Chilblain-like Lesions During the COVID-19 Pandemic. JAMA Dermatol. *157*, 202–206. https://doi.org/10.1001/jamadermatol.2020.4324.
30. Bessis, D., Trouillet-Assant, S., Secco, L.P., Bardin, N., Blanc, B., Blatiere, V., Chable-Bessia, C., Delfour, C., Girard, C., Richard, J.C., et al. (2022). COVID-19 pandemic-associated chilblains: more links for SARS-CoV-2 and less evidence for high interferon type I systemic response. Br. J. Dermatol. *187*, 1032–1035. https://doi.org/10.1111/bjd.21820.
31. Baeck, M., Peeters, C., and Herman, A. (2021). Chilblains and COVID-19: further evidence against a causal association. J. Eur. Acad. Dermatol. Venereol. *35*, e2–e3. https://doi.org/10.1111/jdv.16901.
32. Baeck, M., and Herman, A. (2021). COVID toes: where do we stand with the current evidence? Int. J. Infect. Dis. *102*, 53–55. https://doi.org/10.1016/j.ijid.2020.10.021.
33. Sánchez-García, V., Hernández-Quiles, R., de-Miguel-Balsa, E., Docampo-Simón, A., Belinchón-Romero, I., and Ramos-Rincón, J.M. (2021). Are the chilblain-like lesions observed during the COVID-19 pandemic due to severe acute respiratory syndrome coronavirus 2? Systematic review and meta-analysis. J. Eur. Acad. Dermatol. Venereol. *36*, 24–38. https://doi.org/10.1111/jdv.17672.
34. Frere, J.J., Serafini, R.A., Pryce, K.D., Zazhytska, M., Oishi, K., Golynker, I., Panis, M., Zimering, J., Horiuchi, S., Hoagland, D.A., et al. (2022). SARS-CoV-2 infection in hamsters and humans results in lasting and unique systemic perturbations after recovery. Sci. Transl. Med. *14*, eabq3059. https://doi.org/10.1126/scitranslmed.abq3059.
35. Imai, M., Iwatsuki-Horimoto, K., Hatta, M., Loeber, S., Halfmann, P.J., Nakajima, N., Watanabe, T., Ujie, M., Takahashi, K., Ito, M., et al. (2020). Syrian hamsters as a small animal model for SARS-CoV-2 infection and countermeasure development. Proc. Natl. Acad. Sci. USA *117*, 16587–16595. https://doi.org/10.1073/pnas.2009799117.
36. Sia, S.F., Yan, L.M., Chin, A.W.H., Fung, K., Choy, K.T., Wong, A.Y.L., Kaewpreedee, P., Perera, R., Poon, L.L.M., Nicholls, J.M., et al. (2020). Pathogenesis and transmission of SARS-CoV-2 in golden hamsters. Nature *583*, 834–838. https://doi.org/10.1038/s41586-020-2342-5.
37. Zazhytska, M., Kodra, A., Hoagland, D.A., Frere, J., Fullard, J.F., Shayya, H., McArthur, N.G., Moeller, R., Uhl, S., Omer, A.D., et al. (2022). Non-cell-autonomous disruption of nuclear architecture as a potential cause of COVID-19-induced anosmia. Cell *185*, 1052–1064.e12. https://doi.org/10.1016/j.cell.2022.01.024.
38. Ng, A.T., Moon, J.J., Steidl, O.R., Bussan, H., Tran, J.M., Luong, G., Nihal, A., Kenfield, M., Frere, J., tenOever, B.R., et al. (2022). Pernio and Early SARS-CoV-2 Variants: Natural History of a Prospective Cohort and the Role of Interferon. Br. J. Dermatol. *187*, 617–619. https://doi.org/10.1111/bjd.21693.
39. Halfmann, P.J., Iida, S., Iwatsuki-Horimoto, K., Maemura, T., Kiso, M., Scheaffer, S.M., Darling, T.L., Joshi, A., Loeber, S., Singh, G., et al. (2022). SARS-CoV-2 Omicron virus causes attenuated disease in mice and hamsters. Nature *603*, 687–692. https://doi.org/10.1038/s41586-022-04441-6.
40. Horiuchi, S., Oishi, K., Carrau, L., Frere, J., Møller, R., Panis, M., and tenOever, B.R. (2021). Immune memory from SARS-CoV-2 infection in hamsters provides variant-independent protection but still allows virus transmission. Sci. Immunol. *6*, eabm3131. https://doi.org/10.1126/sciimmunol.abm3131.
41. Serafini, R.A., Frere, J.J., Zimering, J., Giosan, I.M., Pryce, K.D., Golynker, I., Panis, M., Ruiz, A., tenOever, B., and Zachariou, V. (2022). SARS-CoV-2 Airway Infection Results in Time-dependent Sensory Abnormalities in a Hamster Model. Preprint at bioRxiv. https://doi.org/10.1101/2022.08.19.504551.
42. Carrau, L., Frere, J.J., Golynker, I., Fajardo, A., Rivera, C.F., Horiuchi, S., Roonprapunt, T., Minkoff, J.M., Blanco-Melo, D., and tenOever, B. (2023). Delayed engagement of host defenses enables SARS-CoV-2 viremia and productive infection of distal organs in the hamster model of COVID-19. Sci. Signal. *16*, eadg5470.
43. Stein, S.R., Ramelli, S.C., Grazioli, A., Chung, J.Y., Singh, M., Yinda, C.K., Winkler, C.W., Sun, J., Dickey, J.M., Ylaya, K., et al. (2022). SARS-CoV-2 infection and persistence in the human body and brain at autopsy. Nature *612*, 758–763. https://doi.org/10.1038/s41586-022-05542-y.
44. Cassius, C., Merandet, M., Frumholtz, L., Bergerat, D., Samri, A., Grolleau, C., Grzelak, L., Schwartz, O., Yatim, N., Moghadam, P., et al. (2021). Analysis of T-cell responses directed against the spike and/or membrane and/or nucleocapsid proteins in patients with chilblain-like lesions during the COVID-19 pandemic. Br. J. Dermatol. *185*, 1242–1244. https://doi.org/10.1111/bjd.20647.
45. Liu, W., Russell, R.M., Bibollet-Ruche, F., Skelly, A.N., Sherrill-Mix, S., Freeman, D.A., Stoltz, R., Lindemuth, E., Lee, F.H., Sterrett, S., et al. (2021). Predictors of Nonseroconversion after SARS-CoV-2 Infection. Emerg. Infect. Dis. *27*, 2454–2458. https://doi.org/10.3201/eid2709.211042.

46. Ye, Y., Gaugler, B., Mohty, M., and Malard, F. (2020). Plasmacytoid dendritic cell biology and its role in immune-mediated diseases. Clin. Transl. Immunol. *9*, e1139. https://doi.org/10.1002/cti2.1139.
47. Banchereau, J., and Pascual, V. (2006). Type I interferon in systemic lupus erythematosus and other autoimmune diseases. Immunity *25*, 383–392. https://doi.org/10.1016/j.immuni.2006.08.010.
48. Rönnblom, L., and Alm, G.V. (2001). A pivotal role for the natural interferon alpha-producing cells (plasmacytoid dendritic cells) in the pathogenesis of lupus. J. Exp. Med. *194*, F59–F63. https://doi.org/10.1084/jem.194.12.f59.
49. Bertolotti, A., Boniface, K., Vergier, B., Mossalayi, D., Taieb, A., Ezzedine, K., and Seneschal, J. (2014). Type I interferon signature in the initiation of the immune response in vitiligo. Pigment Cell Melanoma Res. *27*, 398–407. https://doi.org/10.1111/pcmr.12219.
50. Blomberg, S., Eloranta, M.L., Cederblad, B., Nordlin, K., Alm, G.V., and Rönnblom, L. (2001). Presence of cutaneous interferon-alpha producing cells in patients with systemic lupus erythematosus. Lupus *10*, 484–490. https://doi.org/10.1191/096120301678416042.
51. Farkas, L., Beiske, K., Lund-Johansen, F., Brandtzaeg, P., and Jahnsen, F.L. (2001). Plasmacytoid dendritic cells (natural interferon- alpha/beta-producing cells) accumulate in cutaneous lupus erythematosus lesions. Am. J. Pathol. *159*, 237–243. https://doi.org/10.1016/s0002-9440(10)61689-6.
52. Ghoreishi, M., Vera Kellet, C., and Dutz, J.P. (2012). Type 1 IFN-induced protein MxA and plasmacytoid dendritic cells in lesions of morphea. Exp. Dermatol. *21*, 417–419. https://doi.org/10.1111/j.1600-0625.2012.01475.x.
53. Ghoreishi, M., Martinka, M., and Dutz, J.P. (2010). Type 1 interferon signature in the scalp lesions of alopecia areata. Br. J. Dermatol. *163*, 57–62. https://doi.org/10.1111/j.1365-2133.2010.09775.x.
54. Chen, K.L., Patel, J., Zeidi, M., Wysocka, M., Bashir, M.M., Patel, B., Maddukuri, S., White, B., and Werth, V.P. (2021). Myeloid Dendritic Cells Are Major Producers of IFN-β in Dermatomyositis and May Contribute to Hydroxychloroquine Refractoriness. J. Invest. Dermatol. *141*, 1906–1914.e2. https://doi.org/10.1016/j.jid.2020.12.032.
55. Wang, M.L., and Chan, M.P. (2018). Comparative Analysis of Chilblain Lupus Erythematosus and Idiopathic Perniosis: Histopathologic Features and Immunohistochemistry for CD123 and CD30. Am. J. Dermatopathol. *40*, 265–271. https://doi.org/10.1097/DAD.0000000000000945.
56. Gracia-Ramos, A.E., Martin-Nares, E., and Hernández-Molina, G. (2021). New Onset of Autoimmune Diseases Following COVID-19 Diagnosis. Cells *10*, 3592. https://doi.org/10.3390/cells10123592.
57. Christensen, R.E., and Jafferany, M. (2022). Association between alopecia areata and COVID-19: A systematic review. JAAD Int. *7*, 57–61. https://doi.org/10.1016/j.jdin.2022.02.002.
58. Rodero, M.P., Pelleau, S., Welfringer-Morin, A., Duffy, D., Melki, I., and Bader-Meunier, B.; FJDM Study Group (2022). Onset and Relapse of Juvenile Dermatomyositis Following Asymptomatic SARS-CoV-2 Infection. J. Clin. Immunol. *42*, 25–27. https://doi.org/10.1007/s10875-021-01119-y.
59. Zacharias, H., Dubey, S., Koduri, G., and D'Cruz, D. (2021). Rheumatological complications of Covid 19. Autoimmun. Rev. *20*, 102883. https://doi.org/10.1016/j.autrev.2021.102883.
60. Schindelin, J., Arganda-Carreras, I., Frise, E., Kaynig, V., Longair, M., Pietzsch, T., Preibisch, S., Rueden, C., Saalfeld, S., Schmid, B., et al. (2012). Fiji: an open-source platform for biological-image analysis. Nat. Methods *9*, 676–682. https://doi.org/10.1038/nmeth.2019.
61. Schneider, C.A., Rasband, W.S., and Eliceiri, K.W. (2012). NIH Image to ImageJ: 25 years of image analysis. Nat. Methods *9*, 671–675. https://doi.org/10.1038/nmeth.2089.
62. Langmead, B., and Salzberg, S.L. (2012). Fast gapped-read alignment with Bowtie 2. Nat. Methods *9*, 357–359. https://doi.org/10.1038/nmeth.1923.
63. Subramanian, A., Tamayo, P., Mootha, V.K., Mukherjee, S., Ebert, B.L., Gillette, M.A., Paulovich, A., Pomeroy, S.L., Golub, T.R., Lander, E.S., and Mesirov, J.P. (2005). Gene set enrichment analysis: a knowledge-based approach for interpreting genome-wide expression profiles. Proc. Natl. Acad. Sci. USA *102*, 15545–15550. https://doi.org/10.1073/pnas.0506580102.
64. Mootha, V.K., Lindgren, C.M., Eriksson, K.F., Subramanian, A., Sihag, S., Lehar, J., Puigserver, P., Carlsson, E., Ridderstrale, M., Laurila, E., et al. (2003). PGC-1alpha-responsive genes involved in oxidative phosphorylation are coordinately downregulated in human diabetes. Nat. Genet. *34*, 267–273. https://doi.org/10.1038/ng1180.
65. Love, M.I., Huber, W., and Anders, S. (2014). Moderated estimation of fold change and dispersion for RNA-seq data with DESeq2. Genome Biol. *15*, 550. https://doi.org/10.1186/s13059-014-0550-8.
66. Grifoni, A., Weiskopf, D., Ramirez, S.I., Mateus, J., Dan, J.M., Moderbacher, C.R., Rawlings, S.A., Sutherland, A., Premkumar, L., Jadi, R.S., et al. (2020). Targets of T Cell Responses to SARS-CoV-2 Coronavirus in Humans with COVID-19 Disease and Unexposed Individuals. Cell *181*, 1489–1501.e15. https://doi.org/10.1016/j.cell.2020.05.015.
67. Dodge, J.T., Doyle, A.D., Costa-da-Silva, A.C., Hogden, C.T., Mezey, E., and Mays, J.W. (2022). Atto 465 Derivative Is a Nuclear Stain with Unique Excitation and Emission Spectra Useful for Multiplex Immunofluorescence Histochemistry. J. Histochem. Cytochem. *70*, 211–223. https://doi.org/10.1369/00221554211064942.
68. Corbett, K.S., Flynn, B., Foulds, K.E., Francica, J.R., Boyoglu-Barnum, S., Werner, A.P., Flach, B., O'Connell, S., Bock, K.W., Minai, M., et al. (2020). Evaluation of the mRNA-1273 Vaccine against SARS-CoV-2 in Nonhuman Primates. N. Engl. J. Med. *383*, 1544–1555. https://doi.org/10.1056/NEJMoa2024671.

STAR★METHODS

KEY RESOURCES TABLE

REAGENT or RESOURCE	SOURCE	IDENTIFIER
Antibodies		
BV421 Mouse Anti-Human CD154	BD Biosciences	Cat# 563886; RRID: AB_2738466
BUV805 Mouse Anti-Human CD3	BD Biosciences	Cat# 612895; RRID: AB_2739277
BUV395 Mouse Anti-Human CD4	BD Biosciences	Cat#: 564724; RRID: AB_2738917
BUV496 Mouse Anti-Human CD8	BD Biosciences	Cat#: 612943; RRID: AB_2916884
PE anti-human CD134 (OX40) Antibody	Biolegend	Cat#: 350004; RRID: AB_10645478
APC anti-human CD137 (4-1BB) Antibody	Biolegend	Cat#: 309810; RRID: AB_830672
PE/Cyanine7 anti-human CD69 Antibody	Biolegend	Cat#: 310912; RRID: AB_314847
Alexa Fluor® 700 anti-human CD14 Antibody	Biolegend	Cat#: 301822; RRID: AB_493747
CD19-A700 (HIB19	Biolegend	Cat#: 302226; RRID: AB_493751
Rat anti Human CD3	Bio-Rad	Cat#: MCA1477; RRID: AB_321245
Rabbit Anti-CLEC4C antibody	Sigma-Aldrich	Cat# HPA029432; RRID: AB_10601259
Rabbit Anti-Interferon gamma antibody	Abcam	Cat# ab9657; RRID: AB_2123314
Mouse anti-HLA-DR antibody	Innovative Research	Cat# 18–0168; RRID: AB_86690
Rabbit anti-MX1 antibody	Abcam	Cat# ab95926; RRID: AB_10677452
Alexa Fluor 647-AffiniPure Fab Fragment Donkey Anti-Rat IgG (H + L)	Jackson ImmunoResearch Labs	Cat# 712-607-003; RRID: AB_2340697
Alexa Fluor® 594 AffiniPure Donkey Anti-Rabbit IgG (H + L)	Jackson ImmunoResearch Labs	Cat# 711-585-152; RRID:AB_2340621
Alexa Fluor 488-AffiniPure Fab Fragment Donkey Anti-Mouse IgG (H + L)	Jackson ImmunoResearch Labs	Cat# 715-547-003; RRID: AB_2340851
Rabbit IgG VisUCyte HRP Polymer Antibody	R&D Systems	Cat# VC003-025
Mouse IgG VisUCyte HRP Polymer Antibody	R&D Systems	Cat# VC001-025
Rat IgG VisUCyte HRP Polymer Antibody	R&D Systems	Cat# VC005-025
Anti-SARS-CoV-1/2 NP protein (clone 1C7C7)	Millipore Sigma	ZMS1075-25UL; RRID:AB_2893327
Goat anti-Mouse IgG (H + L) Cross-Adsorbed Secondary Antibody, HRP	ThermoFisher	A16072; RRID:AB_2763513
Biological samples		
Patient samples (biopsies and blood)	University of Wisconsin-Madison	registered protocols: IRB# 2020-0667
Patient samples (biopsies)	Lausanne University Hospital	registered protocols:
SARS-CoV-2	Biodefense and Emerging Infections Research Resources Repository (BEI Resources)	NR-52281
Vero-E6 Cells	American Type Culture Collection (ATCC)	CRL-1586; RRID:CVCL_0574
Mesocricetus Auratus (Golden Hamster)	Charles River Laboratory	Strain# 049
Chemicals, peptides, and recombinant proteins		
LIVE/DEAD™ Fixable Near-IR Dead Cell Stain Kit	ThermoFisher Scientific	Cat# L10119
BLOXALL® Endogenous Blocking Solution	Vector Laboratories	Cat# SP-6000-100
Alexa Fluor™ 405 NHS Ester (Succinimidyl Ester)	ThermoFisher Scientific	Cat# A30000
Alexa Fluor™ 594 Tyramide Conjugate	ThermoFisher Scientific	Cat# B40957
Alexa Fluor™ 555 Tyramide Conjugate	ThermoFisher Scientific	Cat# B40955
Atto 465 NHS ester	Sigma Aldrich	Cat# 53404
DAPI	Thermo Fisher Scientific	Cat# 62248

(*Continued on next page*)

Continued

REAGENT or RESOURCE	SOURCE	IDENTIFIER
RNAscope™ Probe - V-nCoV2019-S	Advanced Cell Diagnostics, Inc.	Cat# 848561
RNAscope™ Negative Control Probe- DapB	Advanced Cell Diagnostics, Inc.	Cat# 310043
RNAscope™ Positive Control Probe- Hs-PPIB	Advanced Cell Diagnostics, Inc.	Cat# 313901
SuperScript III Reverse Transcriptase	Thermo Fisher Scientific	Cat# 180800093
Dulbecco's Modified Eagle médium (DMEM) (Gibco)	Thermo Fisher Scientific	Cat# 11965118
Fetal Bovine Serum (FBS)	Thermo Fisher Scientific	Cat# 10437028
HEPES	Thermo Fisher Scientific	Cat# 15630080
Penicillin/Streptomycin	Thermo Fisher Scientific	Cat# 15140122
Amicon Ultra-15 Centrifugal Filter Unit	Sigma-Aldrich	Cat# UFC910024
OXOID Agar	Thermo Fisher Scientific	Cat# OXLP0028B
4% Paraformaldehyde	Thermo Fisher Scientific	Cat# J19943.K2
Crystal Violet	Sigma-Aldrich	Cat# V5265
KAPA SYBR Fast qPCR Master Mix	Kapa Biosystems	Cat# KK4602
Oligo(dT)$_{12-18}$ Primer	Thermo Fisher Scientific	Cat# 18418012
Trizol	Thermo Fisher Scientific	Cat# 15596026
Chloroform	Thermo Fisher Scientific	Cat# J67241.AP
Absolute Ethanol, 200 Proof, Molecular Biology Grade	Thermo Fisher Scientific	Cat# T038181000
Isopropanol, 99.5%	Thermo Fisher Scientific	Cat# 383910025
RIPA Buffer	Thermo Fisher Scientific	Cat# 89901
Laemmli Sample Buffer	Bio-Rad	1Cat# 610737EDU
SuperSignal Femto Maximum Sensitivity Substrate	Thermo Fisher Scientific	Cat# 34094
Phosphate Buffered Saline (Gibco)	Thermo Fisher Scientific	Cat# 10010049
Critical commercial assays		
RNAscope™ 2.5 HD Assay - RED	Advanced Cell Diagnostics, Inc.	Cat# 322452
TruSeq Stranded MRNA Library Preparation Kit	Illumina	Cat# 20020594
MycoAlert Mycoplasma Detection Kit	Lonza	Cat# LT07-318
Lysing Matrix A homogenization tubes	MP Biomedicals	Cat# 116910050-CF
FastPrep-24 5G bead beating grinder and lysis system	MP Biomedicals	Cat# 6005500
Deposited data		
GEO	NCBI	GSE232226
Software and algorithms		
ImageJ 2.0.0	Schindelin et al.[60]; Schneider et al.[61]	https://imagej.nih.gov/ij; RRID: SCR_003070
Biorender	Biorender	https://biorender.com/; RRID: SCR_018361
GraphPad Prism 9.3.1	GraphPad	https://www.graphpad.com/scientific-software/prism/; RRID: SCR_002798
NDP.view2	Hamamatsu Photonics	https://www.hamamatsu.com/us/en/product/life-science-and-medical-systems/digital-slide-scanner/U12388-01.html; RRID: SCR_025177
R	The R Foundation	https://www.r-project.org/; RRID:SCR_001905
BaseSpace	Illumina	https://basespace.illumina.com; RRID:SCR_011881
Bowtie2	Langmead and Salzberg[62]	https://bowtie-bio.sourceforge.net/bowtie2/index.shtml; RRID:SCR_016368
Gene Set Enrichment Analysis	Subramanian et al.[63]; Mootha et al.[64]	https://www.gsea-msigdb.org/gsea/index.jsp; RRID:SCR_003199
DESeq2	Love et al.[65]	https://bioconductor.org/packages/release/bioc/html/DESeq2.html; RRID:SCR_015687

RESOURCE AVAILABILITY

Lead contact

Further information and requests for resources and reagents should be directed to and will be fulfilled by the lead contact, Jacqueline W. Mays (jacqueline.mays@nih.gov).

Materials availability

This study did not generate new unique reagents.

Data and code availability

- Bulk RNA-seq data have been deposited at the National Center for Biotechnology Information (NCBI) Gene Expression Omnibus (GEO) and will be made publicly available as of the date of publication under the accession number GSE232226. Microscopy data reported in this paper will be shared by the lead contact upon request.
- This paper does not report original code. All codes were used in this study in alignment with recommendations made by authors of R packages in their respective user guide, which can be accessed at the key resources table.
- Any additional information required to reanalyze the data reported in this paper is available from the lead contact upon request.

EXPERIMENTAL MODEL AND STUDY PARTICIPANT DETAILS

Patients

Human cohorts

Patients seen in the dermatology department at the University of Wisconsin-Madison with clinical diagnosis of pernio with onset during the pandemic were enrolled in this non-interventional observational study from April 2020 to January 2022. Both sexes were included and children and adults with PAP or as healthy volunteers were enrolled, as detailed in Table 1. Controls were matched by age, sex and geography. Subjects included white non-Hispanic and Hispanic, and Asian individuals. The study was approved by the Institutional Review Boards at both the University of Wisconsin-Madison and Lausanne University Hospital. Study design is outlined in Figure 1A. Inclusion criteria included a clinical diagnosis of pernio during the pandemic period. Exclusion criterion included a history of lupus or interferonopathy. Patients with a history of idiopathic pernio were not excluded due to suspicion for shared genetic susceptibility and the possibility that other coronaviruses could have served as pernio triggers in affected patients. In the Wisconsin cohort, blood collection was performed at presentation and/or between 4 and 8 weeks post-pernio onset. A subset of patients consented to skin biopsy of affected tissue at presentation. A single board-certified dermatopathologist scored the degree of inflammation in all samples (absent or mild superficial inflammation was characterized as "low inflammation," and moderate or severe superficial and deep lymphocytic inflammation was characterized as = high inflammation). De-identified archival cases for use as controls were selected from the pathology libraries at the University of Wisconsin and the HUV University Hospital and University of Lausanne (UNIL), Lausanne, Switzerland. In both cohorts, nasopharyngeal PCR and SARS-CoV-2 IgG nucleocapsid antibody testing (ARUP) were performed for clinical care at presentation. In the Wisconsin cohort (n = 54) with peripheral blood only, total antibody ELISA to spike (Thermo- Fisher Scientific, Waltham, MA) was used to profile the adaptive immune response compared to age-, geographically- and sex-matched controls, who were enrolled sequentially at the start of the pandemic. (Figure S1).

METHOD DETAILS

Activation induced marker (AIM) assay

AIM assays, which are based on TCR-dependent upregulation of cell surface proteins OX40, CD69, and CD137 following peptide stimulation by spike peptides,[66] were used as a proxy for virus-specific T-cells. Cryopreserved cells were thawed and washed twice in warm R10 (RPMI +10% heat-inactivated fetal bovine serum). Thawed cells were rested in two mL of R10 and 50 U/mL benzonase for 2 h at 37°C and 5% CO2. After rest, samples were split into four aliquots of one to two million cells in AIM-V media and incubated for 18–24 h with or without stimulation in the presence of CD154-BV421 (TRAP1, BD Biosciences). Cells were stimulated with one of two commercially available overlapping 15mer peptide pools derived from residues 1 to 604 (S1) and 604 to 1,273 (S2) of SARS-CoV-2 spike protein (1 μg/mL/peptide, JPT), or with Concanavalin A (10 μg/mL) as a positive control. As a negative control, cells were incubated with AIM-V + 0.33% DMSO. Following incubation, cells were washed with FACS Buffer (1% PBS +0.5% FBS) and stained with CD3-BUV805 (UCHT1, BD Biosciences), CD4-BUV395 (RPA-T4, BD Biosciences), CD8-BUV496 (RPA-T8, BD Biosciences), OX40-PE (ACT35, Biolegend), CD137-APC (4B4-1, Biolegend), CD69-PE-Cy7 (FN50, Biolegend), CD14-A700 (M2E2, Biolegend), CD19-A700 (HIB19, Biolgend), and Near-IR live/dead (Thermo Fischer). Stained cells were washed and fixed with 2% PFA. Data were acquired on FACS Symphony and analyzed in FlowJo v10.8 Software (BD Life Sciences). Each sample was gated for singlets and lymphocytes based on forward and side scatter followed by live/dead gating. Live $CD3^+CD14^-CD19^-$ populations were selected and separated into $CD4^+$ and $CD8^+$ populations. Cells were considered activated (AIM positive in the readout) if they were $CD137^+OX40^+$ or $CD137^+CD69^+$ for $CD4^+$ and $CD8^+$ populations, respectively.[66] The limit of detection was calculated to be 0.0001% based on the average total number of $CD3^+CD14^-CD19^-$ cells across samples. Activation marker expression in stimulated conditions were corrected for baseline expression by subtracting the percentage of AIM+ cells in unstimulated condition from the paired

stimulated condition. Differences in the percentages of AIM^+CD4^+ and AIM^+CD8^+ cells between the PAP and Control groups were evaluated using two-tailed T-tests with a significance level of 0.05. Statistical and visualization were done in GraphPad Prism 9.3.1.

Tissue analysis

Affected human skin biopsy specimens were formalin-fixed, paraffin-embedded (FFPE) and sectioned prior to histopathologic diagnosis of pernio. Sections were subsequently deparaffinized and rehydrated with a decreasing graded ethanol series. Heat-induced antigen retrieval was done in a pressure pot in either citrate buffer (10 mM, pH 6.0) or Tris–EDTA buffer (10 mM/1 mM, pH 9.0) with 20 min of cooling. For HLA, CD3 and IFNγ staining, slides were blocked with 5% normal donkey serum in PBS for 30 min, followed by incubation of primary antibodies (STAR Methods) in PBS_0.1% BSA overnight. Slides were then rinsed in PBS and incubated with appropriated secondary antibodies (Jackson ImmunoResearch, West Grove, PA) for 30 min at RT in the dark.

The tyramide signal amplification (TSA)-system was employed for CD303, CD3 and MXA staining, as described previously.[67] Briefly, endogenous peroxidase (HRP) activity was blocked with Bloxall (Vector Labs, Burlingame, CA) and tissue sections incubated overnight with primary antibodies (Table S3). Fluorescence detection was achieved with HRP-polymer secondary antibodies and tyramide- Alexa Fluor 405, Alexa Fluor 488, Alexa Fluor 555, Alexa Fluor 594 or Alexa Fluor 647 (Thermo Fisher Scientific). Negative technical controls in which the primary antibody is omitted were included in both traditional and tyramide-based immunofluorescence. Finally, nuclei were counterstained with either Atto 465-p (4 μM)[67] or 4′,6-diamidine-2-phenylindole (1:200; DAPI; Invitrogen) for 5 min at RT, and coverslips were mounted with Fluoro-Gel (Electron Microscopy Sciences, Hatfield, PA).

Tissue sections were scanned using either a Nikon A1R confocal microscope (fitted with a Plan Fluor 40×/1.30 oil objective) using the NIS Elements imaging software (Nikon Instruments Inc., Melville, NY) or a Leica SP8 confocal microscope (fitted with an HC APO CS2 40×/1.30 oil objective) using the Leica Application Suite X (LAS X) software (Leica, Wetzlar, Germany). Images acquired from both Nikon and Leica microscopes were visualized.To avoid any bias in quantification, evaluable imageswith discrete/reliable staining were blinded to group and and quantified using Fiji Is Just ImageJ (Fiji; version 2.0.0). The requirement of evaluable staining in the clinical samples for inclusion in the dataset resulted in the variable number of patients per group in IHC panels, which are detailed as a range in Figure 3.

In situ hybridization (RNAscope)

Ultra-sensitive single-molecule fluorescence RNA-in-situ hybridization was performed on FFPE sections using RNAscope technology[68] using the RNAscope 2.5 HD reagent kit (Cat. No. 322360) according to manufacturer's protocol. The probe v-nCoV2019-S (ACD Biotech, Hayward, CA; Cat. No. 848561) was used to detect positive-sense SARS-CoV-2 RNA from the S gene encoding spike protein. Negative control probe for the DapB gene of *B. subtilis* strain SMY (Cat. No. 310043) and positive control probe for peptidylprolyl isomerase B (cyclophilin B, PPIB) (Cat. No. 313901) were also used. Images were acquired in brightfield using a NanoZoomer S60 Digital slide scanner (Hamamatsu Photonics, Hamamatsu City, Japan). For this assay, positive staining is indicated by red punctate dots present in the nucleus and/or cytoplasm.

Hamster model

Male adult 6–7 week old Syrian Golden Hamsters (*Mesocricetus auratus*) were obtained from Charles River Laboratory. Hamsters were transferred to CDC/USDA-approved Biosafety Level 3 (BSL-3) facilities at Icahn School of Medicine at Mount Sinai (ISMMS) or New York University Langone (NYUL) and allowed to acclimate for at least 7 days prior to experimentation. Hamsters were anesthetized with ketamine/xylazine, and either PBS (Gibco) (100 μL) or 1000 plaque-forming units (pfu) of SARS-CoV-2 (NR-52281) (Biodefense and Emerging Infections Research Resources Repository, BEI Resources) (100 μL) were intranasally administered or intravenously administered via retro-orbital injection. In this longitudinal study, mock-treated or SARS-CoV-2 intranasally infected hamsters were sacrificed at various time points 1-30-day following infection per an Institutional Animal Care and Use Committee-approved protocol. On various days post-infection (dpi) as described in the text, hamsters were euthanized by intraperitoneal injection of pentobarbital and were intracardially perfused with 60 mL PBS. Lungs were harvested directly from exposed thoracic cavity per standard anatomical dissection techniques. Toes were excised from feet of euthanized hamsters and thus included skin, nail, muscle, and bone tissue. Tissues were harvested directly into Trizol (Thermo Fisher Scientific), PBS (Gibco), or Radio-Immunoprecipitation Assay (RIPA) buffer (Thermo Fisher Scientific) in Lysing Matrix A homogenization tubes (MP Biomedicals) and homogenized for 40 s at 6 m/s for 2 cycles in a FastPrep 24 5G bead grinder and lysis system (MP Biomedicals) for RNA isolation, plaque assay, or western blot analysis respectively.

Viruses and plaque assays

SARS-CoV-2 isolate USA-WA1/2020 (NR-52281) (Biodefense and Emerging Infections Research Resources Repository, BEI Resources) was propagated in Vero-E6 cells (American Type Culture Collection, ATCC) grown in Dulbecco's Modified Eagle Medium (DMEM) (Gibco) that was supplemented with 2% fetal bovine serum (FBS), 1 mM 4-(2-hydroxyethyl)-1-piperazineethanesulfonic acid (HEPES) (Lonza Bioscience) and 1% penicillin/streptomycin (Thermo Fisher Scientific). Supernatant from these cultures was harvested and centrifuged with Amicon Ultra-15 Centrifugal filter unit (Sigma-Aldrich) to form virus stocks. Stocks were sequenced to ensure that furin cleavage site was maintained. Viral titers were quantified by plaque assay in Vero-E6 cells cultured in DMEM with 2% FBS, 1 mM HEPES, and 0.7% OXOID agar (Thermo Fisher Scientific). Assays were fixed in 4% paraformaldehyde (PFA) (Thermo Fisher Scientific) for 24 h, and plaques were visualized by crystal violet (Sigma-Aldrich) staining. All viral stocks used in this study were passage 3 or 4 SARS-CoV-2. All cells used for virus creation and plaque

assay in this study were routinely tested for mycoplasma presence using MycoAlert Mycoplasma Detection Kit (Lonza). For plaque assay of toe homogenate, toe and lung tissues homogenized in PBS were directly added to cell cultures in lieu of viral stocks, and protocol was otherwise kept the same as mentioned previously.

RNA extraction and quantitative reverse transcription polymerase chain reaction

RNA was isolated from homogenized samples by standard TRIzol (Thermo Fischer Scientific) and phenol-choloroform extraction (Thermo Fischer Scientific). One microgram of total extracted RNA from each sample was converted to cDNA using the SuperScript III reverse transcriptase (Thermo Fischer Scientific) and oligo(dT) primers (Thermo Fischer Scientific). Quantitative reverse transcription polymerase chain reaction (qRT-PCR) was performed using the KAPA SYBR Fast qPCR Master Mix kit (KAPA Biosystems) on the Thermo Fischer Quantstudio 7 Instrument (Thermo Fischer Scientific). Delta-delta cycle threshold (DDCt) or inverted raw Ct values were used to visualize expression of genes and viral transcripts in infected hamsters relative to mock-infected controls as stated in the main text.

RNA sequencing and analysis

RNA isolated from harvested hamster tissues was submitted to the New York University Biotechnology Center for NovaSeq 6000 sequencing at a depth of 10 million reads per sample. Libraries were prepped using Illumina TruSeq Stranded mRNA kits (Illumina). Sample-deconvoluted FASTQ files were uploaded to BaseSpace (Illumina) using the command line interface. There, files were aligned to the *Mesocricetus auratus* MesAur1.0 reference genomes using the BaseSpace "RNA-Seq Alignment" application. Salmon files from this analysis were downloaded, and comparative differential expression analysis was performed using DESeq2. All genes with a P-adjusted value (padj) of less than 0.1 were considered "Differentially Expressed Genes". Output from differential expression analysis was used to run Gene Set Enrichment Analysis (GSEA) (MacOS Java Application v4.1.0) (made available by the Broad Institute and the University of California) looking for enrichment of Molecular Signatures Database curated gene set C5 with a gene ranking factor of -log10(*p*-value)*sign(log2FoldChange). Viral SARS-CoV-2 transcripts were quantified by aligning reads to the SARS-CoV-2 genome using Bowtie2. All sequencing output was visualized using GraphPad Prism (v9) or the ggplot2 package in R (The R Foundation).

Western blot

All western blots were carried out using standard procedures. Briefly, harvested hamster toes were homogenized in RIPA buffer. Lysate was centrifuged at maximum speed in a benchtop centrifuge, and cleared supernatant was isolated into a new tube. 50 μg of lysate was incubated at 95°C for 10 min in Laemmli sample buffer (Bio-Rad) prior to being run on an SDS-PAGE gel (Bio-Rad) and transferred to a nitrocellulose membrane. Skim milk was used to block membranes for 1 h prior to overnight incubation with primary antibody (1:5000) (anti-SARS-CoV-2 N Protein 1 g/mL, clone 1C7C7) (Millipore Sigma) in 1% milk in Tris-buffered saline with 0.1% Tween (TBST) at 4°C. Blots were incubated in secondary HRP-conjugated antibodies in 1% milk in TBST prior to being developed using FEMTO ECL (Thermo Fisher Scientific) reagent and imaged on a Chemiluminescence digital imager (Bio-Rad Laboratories). 5 μg of cellular lysate from SARS-CoV-2-infected Vero-E6 cells (multiplicity of infection of 1) at 24 h post-infection collected in RIPA buffer was used as a positive control and processed identically alongside hamster toe tissue homogenates.

PBMC isolation

Blood collection and PBMC separation and cryopreservation were performed via standard protocols. Peripheral blood was processed for PBMC isolation within 1–2 h of collection. Following isolation by centrifugation, PBMCs were cryopreserved in heat-inactivated FBS-10% DMSO with approximately 5 million cells per vial. Aliquots were slowly frozen (@ about 1°/minute) with Mr. Frosty to maintain viability, and then the cells were stored −80 until batched assays were performed.

Activation induced marker (AIM) assay

AIM assays, which are based on TCR-dependent upregulation of cell surface proteins OX40, CD69, and CD137 following peptide stimulation by spike peptides,[66] were used as a proxy for virus-specific T-cells. Cryopreserved cells were thawed and washed twice in warm R10 (RPMI Gibco RPMI 1640 Medium (cat: 11875093) + 10% heat-inactivated fetal bovine serum (FBS; Corning Premium Fetal Bovine Serum, cat: MT35015CV) Thawed cells were rested in two mL of R10 and 50 U/mL benzonase (Millipore Sigma cat: E1014-5KU) for 2 h at 37°C and 5% CO2. After rest, samples were split into four aliquots of one to two million cells in AIM-V media (ThermoFisher cat: 12055083) and incubated for 18–24 h with or without stimulation in the presence of CD154-BV421 (TRAP1, BD Horizon BV421 Mouse Anti-Human CD154). Cells were stimulated with one of two commercially available overlapping 15mer peptide pools derived from residues 1 to 604 (S1) and 604 to 1,273 (S2) of SARS-CoV-2 spike protein (1 μg/mL/peptide, JPT), or with 10 μg/mL of Concanavalin A (Sigma-Aldrich cat: C0412) as a positive control. As a negative control, cells were incubated with AIM-V + 0.33% DMSO (Sigma-Aldrich cat: D2650) Following incubation, cells were washed with FACS Buffer (1% PBS +0.5% FBS) and stained with CD3-BUV805 (UCHT1, BD Horizon BUV805 Mouse Anti-Human CD3), CD4-BUV395 (RPA-T4, BD Horizon BUV395 Mouse Anti-Human CD4), CD8-BUV496 (RPA-T8, BD Horizon BUV496 Mouse Anti-Human CD8), OX40-PE (ACT35, Biolegend PE anti-human CD134 (OX40)), CD137-APC (4B4-1, Biolegend APC anti-human CD137), CD69-PE-Cy7 (FN50, Biolegend PE/Cyanine7 anti-human CD69 Antibody), CD14-A700 (M5E2, Biolegend Alexa Fluor 700 anti-human CD14), CD19-A700 (HIB19, Biolegend Alexa Fluor 700 anti-human CD19), and Near-IR live/dead (ThermoFisher Near-IR live/dead cat: L34975). Stained cells were washed and fixed with

2% paraformaldehyde (Fisher Scientific cat: sc-281692). Data were acquired on FACS Symphony (BD Biosciences, San Diego, CA). and analyzed in FlowJo v10.8 Software (BD Life Sciences). Each sample was gated for singlets and lymphocytes based on forward and side scatter followed by live/dead gating. Live $CD3^+CD14^-CD19^-$populations were selected and separated into $CD4^+$ and $CD8^+$ populations. Cells were considered activated (AIM positive in the readout) if they were CD137+OX40+ or CD137+$CD69^+$ for $CD4^+$ and $CD8^+$ populations, respectively 39. The limit of detection was calculated to be 0.0001% based on the average total number of $CD3^+CD14^-CD19^-$cells across samples. Activation marker expression in stimulated conditions were corrected for baseline expression by subtracting the percentage of AIM+ cells in unstimulated condition from the paired stimulated condition. Differences in the percentages of AIM+$CD4^+$ and AIM+$CD8^+$ cells between the PAP and Control groups were evaluated using two-tailed T-tests with a significance level of 0.05. Statistical and visualization were done in GraphPad Prism 9.3.1.

Immunohistochemistry

Affected human skin biopsy specimens were formalin-fixed, paraffin-embedded (FFPE) and sectioned prior to histopathologic diagnosis of pernio. Sections were subsequently deparaffinized and rehydrated with a decreasing graded ethanol series. Heat-induced antigen retrieval was done in a pressure pot in either citrate buffer (10 mM, pH 6.0) or Tris–EDTA buffer (10 mM/1 mM, pH 9.0) with 20 min of cooling. For HLA-DR (1:000, Zymed), CD3 (1:500, Bio-Rad) and IFNγ (1:100, Abcam) staining, slides were blocked with 5% normal donkey serum in PBS for 30 min, followed by incubation of primary antibodies in PBS_0.1% BSA overnight. Slides were then rinsed in PBS and incubated with appropriated secondary antibodies (Jackson ImmunoResearch) for 30 min at RT in the dark.

The tyramide signal amplification (TSA)-system was employed for CD303 (1:500, Sigma-Aldrich), CD3 (1:2000, Bio-Rad) and MXA (1:500, Abcam) staining, as described previously 76. Briefly, endogenous peroxidase (HRP) activity was blocked with Bloxall (Vector Labs) and tissue sections incubated overnight with primary antibodies. Fluorescence detection was achieved with HRP-polymer secondary antibodies and tyramide- Alexa Fluor 405, Alexa Fluor 488, Alexa Fluor 555, Alexa Fluor 594 or Alexa Fluor 647 (Thermo Fisher Scientific). Negative technical controls in which the primary antibody is omitted were included in both traditional and tyramide-based immunofluorescence. Finally, nuclei were counterstained with either Atto 465-p (4 μM) 76 or 4′,6-diamidine-2-phenylindole (1:200; DAPI; Invitrogen) for 5 min at RT, and coverslips were mounted with Fluoro-Gel (Electron Microscopy Sciences).

Tissue sections were scanned using either a Nikon A1R confocal microscope (fitted with a Plan Fluor 40×/1.30 oil objective) using the NIS Elements imaging software (Nikon Instruments Inc.) or a Leica SP8 confocal microscope (fitted with an HC APO CS2 40×/1.30 oil objective) using the Leica Application Suite X (LAS X) software Leica). To avoid any bias in quantification, images with discrete/reliable staining were processed and quantified using Fiji Is Just ImageJ (Fiji; version 2.0.0), leading to variable number of patients in different IHC panels.

In situ hybridization (RNAscope)

Ultra-sensitive single-molecule fluorescence RNA-in-situ hybridization was performed on FFPE sections using RNAscope technology 77 using the RNAscope 2.5 HD reagent kit (ACD Biotech) according to manufacturer's protocol. The probe v-nCoV2019-S (ACD Biotech) was used to detect positive-sense SARS-CoV-2 RNA from the S gene encoding spike protein. Negative control probe for the DapB gene of *B. subtilis* strain SMY (ACD Biotech) and positive control probe for peptidylprolyl isomerase B (cyclophilin B, PPIB) (ACD Biotech) were also used. Images were acquired in brightfield using a NanoZoomer S60 Digital slide scanner (Hamamatsu Photonics). For this assay, positive staining is indicated by red punctate dots present in the nucleus and/or cytoplasm.

QUANTIFICATION AND STATISTICAL ANALYSIS

Statistical tests as described in the results and figure legends were carried out using GraphPad Prism version 8.4.1 software. Data were generally non-normally distributed, therefore non-parametric statistics were used for most tests to address non-normal sample distribution. The n in all tests indicates the number of unique participants. Alpha was set at 0.05 for all tests except where correction for multiple comparisons was applied, when a smaller alpha was used, which is marked in the description of the test. Differences were considered significant at $p < 0.05$. For RNA-sequencing, all differential expression analysis was conducted in DESeq2, and pathway analysis was carried out in GSEA. Statistical thresholds for each of these tests were described previously (see "RNA sequencing and analysis").

ADDITIONAL RESOURCES

Additional study details for recruitment were on the UW-Madison Department of Dermatology website: https://dermatology.wisc.edu/research/clinical-research/#Recruiting.